

## JAXA Research and Development Report

---

Pressure Gradient Effects on Transition Location over  
Axisymmetric Bodies at Incidence in Supersonic Flow

- Progress Report of JAXA-NASA Joint Research Project  
on Supersonic Boundary Layer Transition (Part 2) -

Naoko Tokugawa, Yoshine Ueda, Hiroaki Ishikawa, Keisuke Fujii,  
Meelan Choudhari, Fei Li, Chau-Lyan Chang and Jeffery White

September 2017

Japan Aerospace Exploration Agency

**Pressure Gradient Effects on Transition Location over Axisymmetric  
Bodies at Incidence in Supersonic Flow  
- Progress Report of JAXA-NASA Joint Research Project  
on Supersonic Boundary Layer Transition (Part 2) -**

Naoko Tokugawa <sup>\*1</sup>, Yoshine Ueda <sup>\*2</sup>, Hiroaki Ishikawa <sup>\*3</sup>, Keisuke Fujii <sup>\*1</sup>,  
Meelan Choudhari, <sup>4</sup>Fei Li <sup>\*4</sup>, Chau-Lyan Chang <sup>\*4</sup> and Jeffery White <sup>\*4</sup>

**ABSTRACT**

Boundary layer transition along the leeward symmetry plane of axisymmetric bodies at nonzero angle of incidence in supersonic flow was investigated numerically as part of joint research between the Japan Aerospace Exploration Agency (JAXA) and the National Aeronautics and Space Administration (NASA). Stability of the boundary layer over five axisymmetric bodies (namely, the Sears-Haack body, the semi-Sears-Haack body, two straight cones and the flared cone) was analyzed in order to investigate the effects of axial pressure gradients, freestream Mach number and angle of incidence on the boundary layer transition. Moreover, the transition location over four bodies was detected experimentally. The strong effects of axial pressure gradients on the boundary layer profiles along the leeward ray, including an earlier transition under adverse axial pressure gradients, were indicated in both numerical predictions and experimental measurements. The destabilizing effect of the pressure gradient on the boundary layer flow within the leeward symmetry plane is shown to be related to the three-dimensional dynamics involving an increasing build-up of secondary flow along the leeward symmetry plane under an adverse axial pressure gradient. A detailed description of the mean flow computation, which forms the basis for the present linear stability analysis, is provided in an accompanying report that forms part 1 of this document.

**Keywords:** 3-D Boundary Layer, Transition, Stability Analysis, Experiment

---

doi: 10.20637/JAXA-RR-17-003E/0001

\* Accepted December 8, 2015, Received June 8, 2017

<sup>\*1</sup> Aeronautical Technology Directorate, Japan Aerospace Exploration Agency

<sup>\*2</sup> TRYANGLE Inc.

<sup>\*3</sup> ASIRI Inc.

<sup>\*4</sup> Computational Aero Sciences Branch, NASA Langley Research Center

## Contents

<b>Nomenclature</b> .....	<b>4</b>
<b>1 Introduction</b> .....	<b>5</b>
<b>2 Model Geometry and Flow Conditions</b> .....	<b>7</b>
<b>3 Summary of Mean Flow Computations</b> .....	<b>10</b>
3.1 Computational Methodologies .....	10
3.2 Surface Pressure Distributions and Mean Velocity Profiles .....	11
<b>4 Methodologies and Results of Stability Analysis</b> .....	<b>14</b>
4.1 Maximum Growth Envelope Method .....	14
4.2 Mode Tracking Method .....	14
4.3 Results of the Maximum Growth Envelope Method .....	14
4.4 Comparison of Stability Analysis .....	18
<b>5 Method and Results of Experiments</b> .....	<b>20</b>
5.1 Wind Tunnel Facilities .....	20
5.2 Test Models .....	21
5.3 Instrumentation and Measurement Methodologies .....	23
5.4 Pattern of Heat Transfer Distribution .....	25
5.5 Extraction of Transition Location .....	29
5.6 Comparison with numerical prediction .....	30
<b>6 Summary</b> .....	<b>35</b>
<b>Acknowledgments</b> .....	<b>36</b>
<b>References</b> .....	<b>37</b>
<b>Appendix A: Identification of transition location from surface temperature distribution</b> .....	<b>42</b>
<b>Appendix B: Identification of transition location from surface temperature distribution</b> .....	<b>45</b>

## Nomenclature

$C$	=	heat capacitance of polysulfone [J/K]
$C_p$	=	surface pressure coefficient $(p - p_\infty)/([1/2] \rho_\infty U_\infty^2)$
$L$	=	model length [m]
$M$	=	Mach number
$N$	=	logarithmic amplification ratio of instability waves relative to the station where they first begin to amplify
$p$	=	pressure [Pa]
$p'_{\text{RMS}}$	=	root-mean-square static pressure fluctuation scaled by $[1/2] \rho_\infty U_\infty^2$ , the dynamic pressure in free-stream [Pa]
$q_w$	=	heat flux across model wall [W/m <sup>2</sup> ]
$R(x)$	=	local radius at axial location $x$ [m]
$Re_{\text{unit}}$	=	unit Reynolds number
$Re_x$	=	local Reynolds number based on free-stream velocity and kinematic viscosity
$Re_{x,tr}$	=	local Reynolds number based on free-stream velocity and kinematic viscosity at transition location
$t$	=	time [s]
$T$	=	temperature [K]
$U$	=	velocity [m/s]
$x$	=	axial location with respect to cone apex [m]
$\alpha$	=	angle of incidence [deg]
$\delta$	=	boundary layer thickness [mm]
$\kappa$	=	thermal conductivity [W/(m·K)]
$\varphi$	=	circumferential (i.e., azimuthal) angle with respect to the leeward plane of symmetry [deg]
$\rho$	=	density [kg/m <sup>3</sup> ]
$\psi$	=	the angle of wave number vector of the most amplified disturbance mode with respect to inviscid streamline at the body surface [deg]
FC	=	flared cone
SC	=	straight cone
SH	=	Sears-Haack body
SSH	=	semi Sears-Haack body
0	=	stagnation condition
$\infty$	=	free-stream condition

## 1 Introduction

The Japan Aerospace Exploration Agency (JAXA) and the National Aeronautics and Space Administration (NASA) have been promoting a joint research program on the boundary layer transition in supersonic flow. The attention is paid to the transition phenomena along the leeward symmetry plane of axisymmetric bodies at nonzero angle of incidence as the first topic of the joint research program. The objective of this research program is to improve the knowledge base for transition mechanisms relevant to the nose region of the fuselage.

Although the main parts of results are already published [1-3], the detailed results are going to be reported in 2 separate papers. And the progress on the mean flow computation has been already submitted as part 1 of the detailed reports [4]. In the present paper, the investigations of stability analysis and experiment are addressed for the combined effects of angle-of-incidence and axial pressure gradient on boundary layer transition over canonical shapes of axisymmetric bodies, with an emphasis on transition characteristics near the leeward plane of symmetry.

Although the background of this research has been described in the separate reports [1-4], it is summarized here briefly.

Drag reduction is one of the most important technical problems for aircraft, and has been extensively investigated over the years [5-43]. The potential for further improvement in aerodynamic efficiency via natural laminar flow (NLF) over the fuselage surface, especially near the nose of the aircraft, is increasing.

As the basic shape of the fuselage, transition in boundary layers on axisymmetric bodies in supersonic flow has been extensively studied in the literature [44-60]. Despite the simplicity of the body shape, supersonic flow over a straight cone with a circular cross section is known to exhibit a rich transition behavior. At nonzero angles of incidence, the boundary layer becomes three dimensional and the inviscid streamlines at the surface become curved due to the azimuthal pressure gradient from the windward to the leeward side. Therefore, crossflow occurs and the boundary layer over the side region becomes increasingly susceptible to crossflow instability as the angle of incidence is increased. Even at a finite angle of incidence, supersonic boundary layer flow along the windward symmetry plane has been shown to exhibit a nearly self-similar behavior and, furthermore, the instability amplification within this plane has been shown to remain dominated by first mode instability.

It is well-known from the early work on supersonic flow past straight cones [56] that, the boundary layer flow along the leeward plane of symmetry evolves rather differently than elsewhere on the cone surface. Specifically, the convergence of low-speed secondary flow from both sides of the leeward symmetry plane leads to a lift-up effect within the plane of symmetry, and hence to a significant thickening of the boundary layer along the leeward plane. The thicker boundary layer profiles exhibit a strong inflectional behavior, and hence are more unstable than the boundary layer flow in the adjoining region of the cone.

Preliminary computations showed that the boundary layer profiles along the leeward symmetry plane are highly sensitive to the magnitude of the axial pressure gradient. When the pressure gradient along the leeward ray is favorable, such as for the flow past the Sears-Haack body at a small angle of incidence, the lift-up effect within the leeward symmetry plane is substantially reduced. The accelerated axial flow carries the low-speed fluid converging from both sides of the leeward plane. Consequently, the velocity profiles along the leeward ray can remain noninflectional, resulting in a more stable boundary layer flow. This alters the relative locations of transition location along the leeward plane and the earliest location of crossflow-induced transition over the side of the cone. Indeed, major changes in the transition front characteristics can occur as the body shape is varied. An understanding of these changes is relevant to the aerodynamic design of an aircraft nose targeting a longer region of NLF.

Transition fronts with three local minima, one along the leeward ray and one each due to crossflow transition on either side have previously been observed and/or predicted in the context of straight cones [48-56] and a delta wing configuration [43]. However, the physics of transition along the leeward plane and the effect of axial pressure gradient on the corresponding transition location has not been scrutinized in detail, perhaps due to the narrow width of the transition lobe centered on the leeward ray and/or the reduced wall shear stress associated with the thicker boundary layer in that region. The latter factors aside, the ubiquitous nature of analogous transition patterns in the context of fully 3D high-speed flows over slender bodies [58, 59] makes it even more useful to examine the transition process along the leeward symmetry plane in greater detail.

The following section introduces the five different axisymmetric bodies with varying axial pressure gradients, which were used during the present investigation. And the studies of mean flow computation are summarized in Section 3. Then Methodologies and results of stability analysis are described in Section 4. The experimental method and the experimental results are described in Section 5. A summary of the present work and concluding remarks are presented in Section 6.

## 2 Model Geometry and Flow Conditions

The five different axisymmetric bodies targeted in the present investigation are the Sears-Haack body, a semi-Sears-Haack body, two straight cones, and a flared cone. Those geometries were selected according to the condition of experiments that had been conducted independently in each institute. Although the geometry has been described in detail in the former reports [1-4], it should be explained here again in order to be constructed as an independent report.

The shapes of all five bodies are plotted in Fig. 1, wherein  $x$  denotes the axial coordinate relative to the cone apex and  $R$  represents the local body radius at a given station.  $\varphi$  denotes the azimuthal directions.  $\varphi = 0$  degree corresponds to the leeward symmetric plane, and  $\varphi = 180$  degree corresponds to the windward symmetric plane.

The total length in axial direction  $L$  is confined to  $L = 0.33$  m corresponding to the experiments.

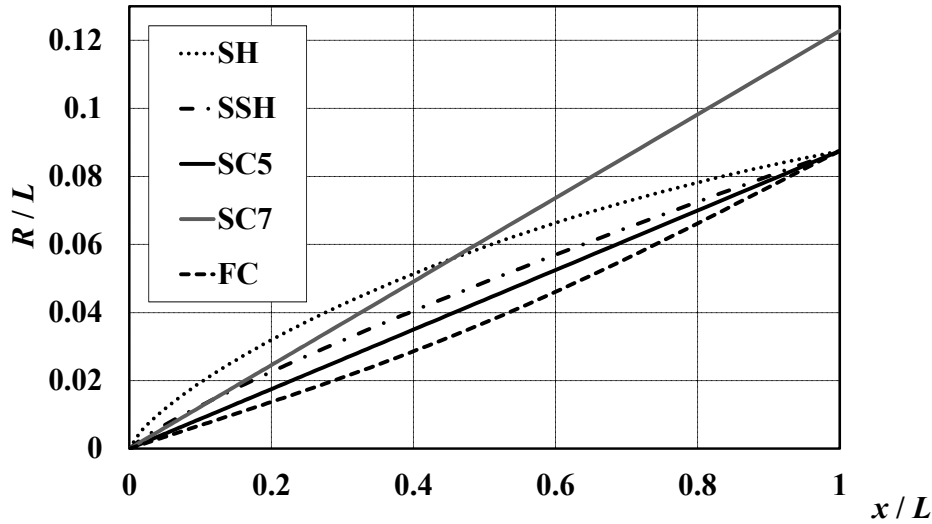


Figure 1. Geometry of selected axisymmetric shapes [4].

The Sears-Haack body (abbreviated as SH in the following) produces the least wave drag for a given length and maximum diameter based on slender body theory. Its shape is defined by the following expression for the axial distribution of local body radius  $R_{SH}(x)$ :

$$R_{SH}(x) = A_0[(x/L_{SH})\{1 - (x/L_{SH})\}]^{(3/4)}, \quad (1)$$

where  $L_{SH}(x) = 1.194938$ m and  $A_0(x) = 0.09657$  m. However, the object of analysis is the nose region with a length of  $L = 0.33$  m.

The semi-Sears-Haack body (abbreviated as SSH in the following) corresponds to a linearly weighted mean of the radius distributions for the Sears-Haack body and a straight cone, as expressed by the radius distribution  $R_{SSH}(x)$ :

$$R_{SSH}(x) = 0.3 \times R_{SH}(x) + 0.7 \times R_{SC}(x), \quad (2)$$

where  $R_{SC}(x)$  corresponds to the local radius of the straight cone with 5 degrees in the cone half-angle as defined below. The weighting coefficients was chosen precisely via linear stability

two cases.

The straight cone geometry is defined by the cone half-angle, which is equal to 5 degrees or 7 degrees for the present study. The variation of model radius with the axial coordinate is defined as follows:

$$R_{SC}(x) = x \tan \theta. \quad (3)$$

The straight cones are collectively named SC, and those with 5 degrees and 7 degrees in the cone half-angle are individually abbreviated as SC5 and SC7, respectively, in the following.

Finally, the flared cone (abbreviated as FC in the following) geometry is defined by the following distribution of model radius:

$$R_{FC}(x) = \begin{cases} -1.0478 \times 10^{-9}x^4 + 6.9293 \times 10^{-7}x^3 - 6.1497 \times 10^{-5}x^2 + 6.998 \times 10^{-2}x - 6.2485 \times 10^{-4} & (x > 0), \\ 0 & (x = 0) \end{cases} \quad (4)$$

where the axial coordinate  $x$  is measured in meters.

**Table 1: Summary of flow conditions and case notation.**

Geometric Configuration	Flow Condition			
	2.0		3.5	
Mach number $M_\infty$	2.0		3.5	
stagnation pressure $P_0$	99.0kPa	70.0 kPa	175.8kPa	344.8kPa
stagnation temperature $T_0$	297.0K	335 K	300K	300K
free-stream pressure $P_\infty$	12.65kPa	8.95kPa	2.305 kPa	4.521 kPa
free-stream temperature $T_\infty$	165.0K	186 K	86.96K	86.96K
free-stream density $\rho_\infty$	0.2671kg/m <sup>3</sup>	0.1675kg/m <sup>3</sup>	0.09234kg/m <sup>3</sup>	0.1811kg/m <sup>3</sup>
unit Reynolds number $R_{unit}/m$	12.23 × 10 <sup>6</sup>	7.32 × 10 <sup>6</sup>	10.08 × 10 <sup>6</sup>	19.75 × 10 <sup>6</sup>
angle of incidence $\alpha$	0deg	2deg	0deg	4.2deg
Sears-Haack body (SH)	/	SH-2deg-99	SH-2deg-70	/
semi-Sears-Haack body (SSH)		SSH-2deg-99	SSH-2deg-70	
straight cone with 5-degree half angle (SC5)	SC5-0deg-99	SC5-2deg-99	SC5-2deg-70	
straight cone with 7-degree half angle (SC7)	/		SC7-0deg-176	
flared cone (FC)	/	FC-2deg-99	FC-2deg-70	/

The semi-Sears-Haack body and flared cone configurations were originally designed at JAXA for investigating the influence of pressure gradient on the flow characteristics near the leeward symmetry plane [57].

Table 1 provides the summary of studied cases as well as introducing a composite notation that combines the information about the shape, angle-of-incidence, and stagnation pressure. For example, the case SC5-0deg-99 from Table 1 refers to the straight cone with 5-degree half angle SC at 0-degree incidence and a stagnation pressure of 99 kPa.

The values of stagnation pressure correspond to the experimental conditions, which are conducted by JAXA. The quantities  $M_\infty$ ,  $P_0$ ,  $T_\infty$ , and  $Re_{\text{unit}}$  denote the Mach number, stagnation pressure, static temperature, and unit Reynolds number, respectively, of the oncoming freestream. The flow conditions are nominal value in a series of experiments.

### 3 Summary of Mean Flow Computations

The results of mean flow computations, which were conducted at JAXA and NASA, are compared with each other. Then, it is confirmed that those are in fairly good agreement with each other. Even though, there were observed slight differences due to thermal condition, numerical grid and computational solver. The difference due to the thermal condition is obvious but reasonable, and the other differences are very small. Moreover, the JAXA grid is confirmed to be sufficient in order to apply to the linear stability analysis, though the JAXA grid is coarser than the NASA grid.

The investigation of mean flow computations [1-4] is summarized below.

#### 3.1 Computational Methodologies

The laminar basic state at each condition was obtained using numerical solutions to the compressible Navier-Stokes equations. Due to the long duration of the tests, the test model reaches thermal equilibrium with the surrounding flow and, hence, the thermal boundary condition at the model surface corresponds to an adiabatic wall. On the other hand, an isothermal boundary condition is more appropriate for the short duration tests corresponding to a higher stagnation pressure ( $P_0 = 99$  kPa) in the FWT (the 0.6m×0.6m High Speed Wind Tunnel at Fuji Heavy Industries in Japan). For the FWT test conditions, the estimated recovery temperature (based on a recovery factor of 0.85) is 277 K. Thus, the isothermal model temperature of  $T_w = 300$  K used for the mean flow computations corresponds to  $T_w/T_{ad} \approx 1.08$ .

Two different flow solvers were used for this purpose and extensive comparisons were made between the respective solutions to ensure that the computed mean flow solutions were independent of the code. Computations with adiabatic thermal wall boundary conditions were performed using the 3D, multi-block, structured-grid flow solver UPACS [61], which was developed at JAXA. Independent computations for the same test conditions were performed at NASA using an analogous 3D, multi-block, structured-grid flow solver, VULCAN [62] that was developed at the NASA Langley Research Center. Additional computations were done with the VULCAN code to compute the basic state solutions corresponding to the isothermal wall boundary condition ( $T_w = 300$  K).

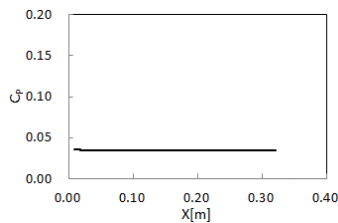
The computational grids were also independently generated based on knowledge and experience. The UPACS based computations at JAXA were based on a typical grid size of 120 points in the axial direction, 150 points in the surface normal direction, and more than 193 points in the azimuthal (i.e., circumferential) direction. On the other hand, computations at NASA were based on a typical grid size of 610 points in the axial direction, 353 points in the surface normal direction, and more than 257 points in the azimuthal direction. The wall-normal grid distribution was similar for both flow solvers. The nose radius of each axisymmetric configuration was assumed to be zero for the UPACS computations, whereas the VULCAN computations used a nonzero but tiny nose radius (approximately 4  $\mu\text{m}$ ) that was resolved with approximately 65 axial points in the nose region. The number of points in the JAXA computational grid is much less. However, the result showed that the JAXA grid appropriate for the necessary resolution required.

### 3.2 Surface Pressure Distributions and Mean Velocity Profiles

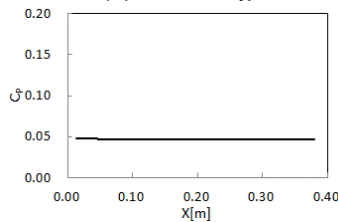
Figures 2(a) through 2(g) display the surface pressure distributions for each body shape and angle of incidence that were obtained at adiabatic thermal wall boundary conditions by use of UPACS.

Regardless of the body shape, a positive azimuthal pressure gradient was observed at any fixed axial station at nonzero angle of incidence cases. The azimuthal pressure gradient drives a circumferential flow from the windward to the leeward side and, hence, causes the boundary layer flow to become fully three-dimensional. On the other hand, the pressure gradient in the axial direction varies with the body shape. As alluded to previously, it is favorable along the SH and SSH body shapes, but almost zero for the SC shapes and adverse for the FC. The favorable pressure gradient along the length of the SSH body is weaker in comparison with that along the SH body. In comparison with two straight cones, it was found that the pressure distribution of SC7-0deg-176 case is qualitatively almost the same as that of the SC5-0deg-99 case, as expected by linear theory for slender bodies. However, the azimuthal pressure gradient of the SC7-4.2deg-345 case is much larger than that of the SC5-2deg-99 case.

The axial development of the mean velocity profiles along a generatrix at zero-degree angle of incidence, i.e., SC5-0deg-99 and SC7-0deg-176 cases, are virtually self-similar (Fig. 3(a) and Fig. 3(b)). On the other hand, the leeward plane profiles in the SH-2deg-99 case continue to develop in the axial direction and are not self-similar. The variation in velocity profiles over a similar range of locations becomes stronger as the magnitude of the favorable pressure gradient in the axial direction is reduced from the SH body shape (Fig. 3(c)) to the SSH body shape (Fig. 3(d)).

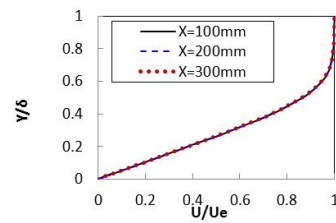


(a) SC5-0deg-99

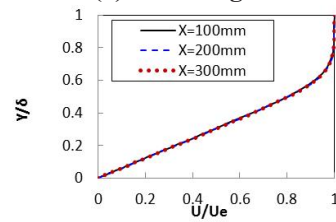


(b) SC7-0deg-176

Figure 2. Surface pressure distribution [1-4].



(a) SC5-0deg-99



(b) SC7-0deg-176

Figure 3. Mean velocity profiles along the leeward ray [1-4].

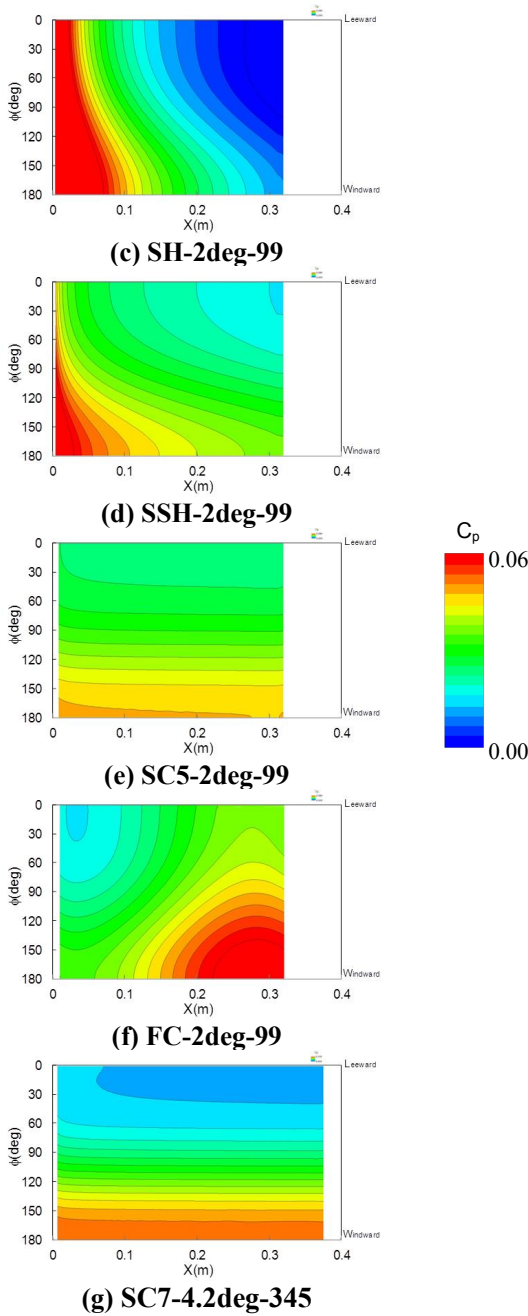


**Figure 2. Surface pressure distribution [1-4].  
(completed)**

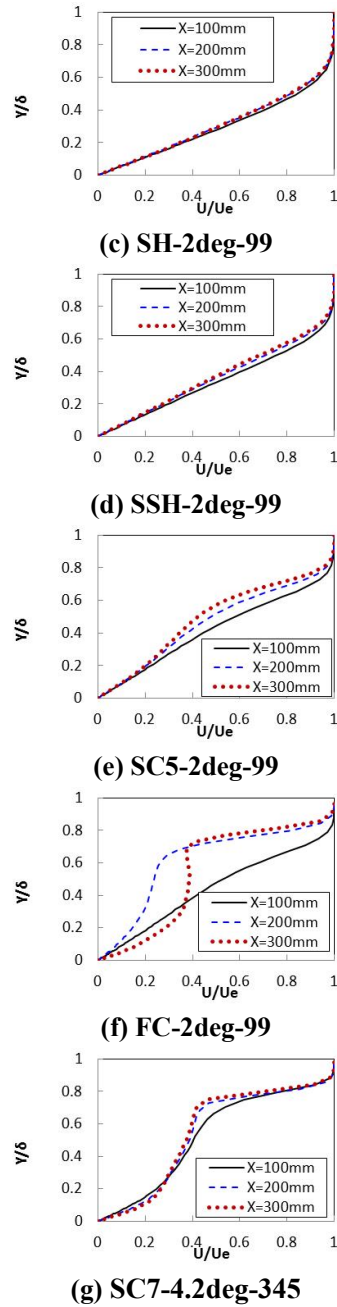


**Figure 3. Mean velocity profiles along the leeward ray [1-4].  
(completed)**

As shown in Fig. 3, the existence of inflection is even visually obvious in the case of velocity profiles along the leeward ray of the SC5-2deg-99 configuration (Fig. 3(e)). The characteristics are stronger for SC7-4.2deg-345 (Fig. 3(g)) case. And the inflection becomes also stronger when the axial pressure gradient becomes negative (case FC-2deg-99 in Fig. 3(f)). The lift-up effect increases as the axial location moves downstream.

The velocity profiles on the sides and along the windward ray are compared with that along the leeward ray for SC5-2deg-99 case (Fig. 4). The profiles along the windward ray are virtually self-similar as seen from the collapse. On the other hand, it is confirmed that the existence of inflection is even visually obvious in the case of velocity profiles along the leeward ray.

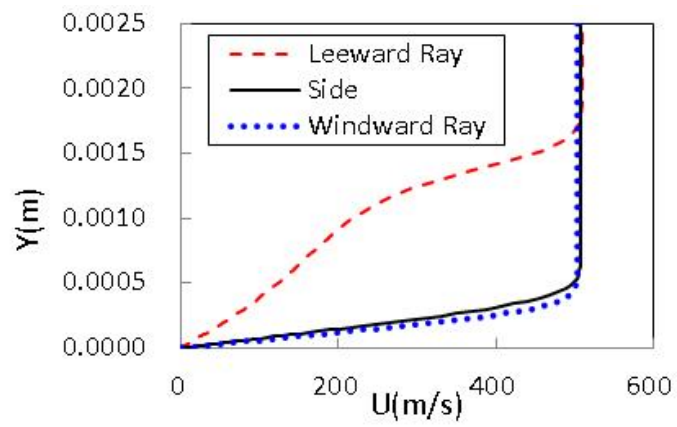


**Figure 4. Mean velocity profiles of SC5-2deg-99 case at [4].**

## 4 Methodologies and Results of Stability Analysis

The laminar mean flows described in the previous section were used as basic states for linear stability analysis to understand the measured transition characteristics near the leeward ray. Computations were performed using the LSTAB [55] code developed at JAXA and the LASTRAC [63] code developed at the NASA Langley Research Center. The growth rates were integrated along selected trajectories along the cone surface to enable a comparison between predicted  $N$ -factors (i.e., logarithmic amplification ratios) for unstable disturbances with the observed transition fronts. A selected set of results based on the  $e^N$  methodology is described below.

### 4.1 Maximum Growth Envelope Method

The maximum growth envelope method correlates the transition location with the logarithmic amplification ratio (i.e.,  $N$ -factor) based on the most amplified fixed frequency disturbance. For each frequency, the  $N$ -factor distribution over the body surface is determined by integrating the maximum growth rate over all azimuthal wave numbers at each point along a selected set of trajectories. In this paper, these trajectories are taken to be streamlines near the edge of the boundary layer.

### 4.2 Mode Tracking Method

An alternative to the maximum growth envelope method for  $N$ -factor correlations is the mode tracking method. Rather than maximizing the local growth rate over all disturbance wave numbers at a given frequency, the mode tracking method uses the maximum growth envelope of several  $N$ -factor curves, each of which corresponds to a nominally fixed disturbance entity in the form of a specified set of frequency-azimuthal wave number (i.e.,  $(f, n)$  a combination (of specific disturbance modes). Stability computations using the mode tracking approach were performed using the LASTRAC code.

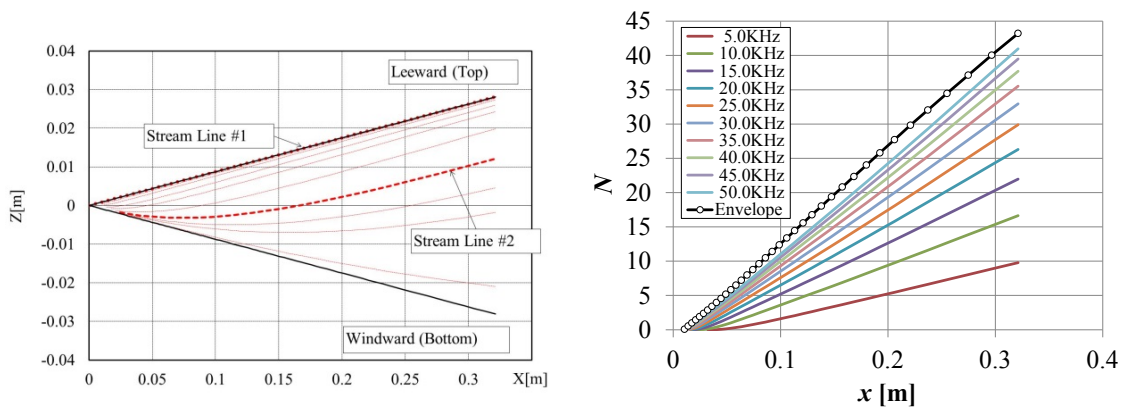
### 4.3 Results of the Maximum Growth Envelope Method

The growth of a disturbance was traced along two typical stream lines on the SC5-2deg-99 case (Fig. 5). The first stream line (abbreviated as #1 in the following) is that along the leeward symmetry plane. And the second one (abbreviated as #2 in the following) along the side line (a generatrix at  $\varphi = 90$  deg) at  $x \approx 0.2$  m.

The growth rate along the leeward symmetry plane (the stream line #1) increased monotonically (Fig. 5(b)). And the growth rate is larger for the high frequency component. On the other hand, the growth rate along the stream line #2 for a fixed frequency increased once, then it was saturated (Fig. 5(c)). And the frequency of the most increased component changed with the axial location. The behavior of growth rate like the one for stream line #1 was limited to the stream lines #1 (Fig. 5(d)). These results suggest that the transition mechanism for stream line #1 differ from those for the other stream lines. Similar behavior was observed for the other configurations.

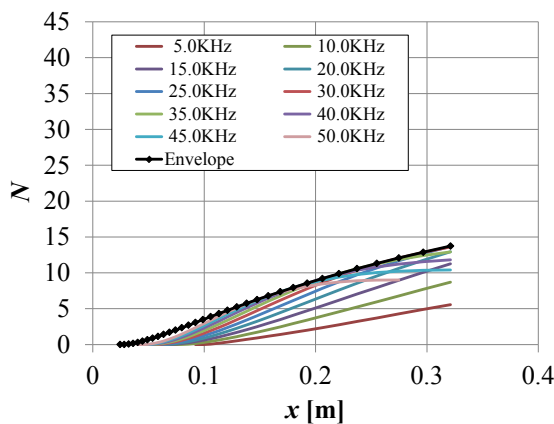
$N$ -factor contours corresponding to LSTAB computations based on the UPACS mean flow solutions for 2-degrees angle of incidence and both values of stagnation pressure in Table 1 ( $P_0 = 99$  kPa and  $P_0 = 70$  kPa cases) were included in Figs. 6(a) through 6(h). And those for SC5-0deg-99, SC7-0deg-176 and SC7-4.2deg-345 cases are also shown in Figs. 6(i), 6(j) and 6(k). As expected, an azimuthally invariant transition front is predicted in the SC5-0deg-99 case and SC7-0deg-176 cases.

$N$ -factor contours for the SH body at nonzero angle of incidence predict a later transition location along the leeward symmetry plane than the neighboring azimuthal locations (Figs. 6(a) and 6(b)). In contrast, computations for the other 4 body shapes (Figs. 6(b) through 6(h) and 6(k)) predict a 3-lobed transition front including a center lobe that is indicative of an earlier transition location along the leeward ray in comparison with the adjacent azimuthal locations. The center lobe moves progressively farther upstream as the axial pressure gradient changes from mildly favorable (SSH) to nearly zero (SC) to adverse (FC). This upstream movement of transition location along the leeward ray is attributed to the higher amplification rates associated with increasingly thicker, and highly inflectional velocity profiles along the leeward symmetry plane (Fig. 3).

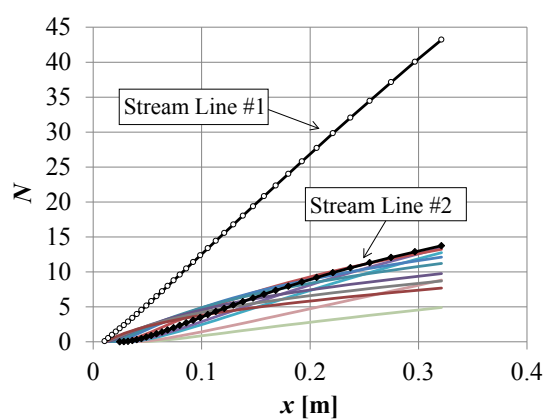


(a) Illustration of streamlines on the model in the SC5-0deg-99 case.

(b) Growth rate predicted along the stream line #2.



(c) Growth rate predicted along the stream line #1.



(d) Growth rate predicted along each stream lines.

Figure 5. Growth rate for the SC5-0deg-99 case.

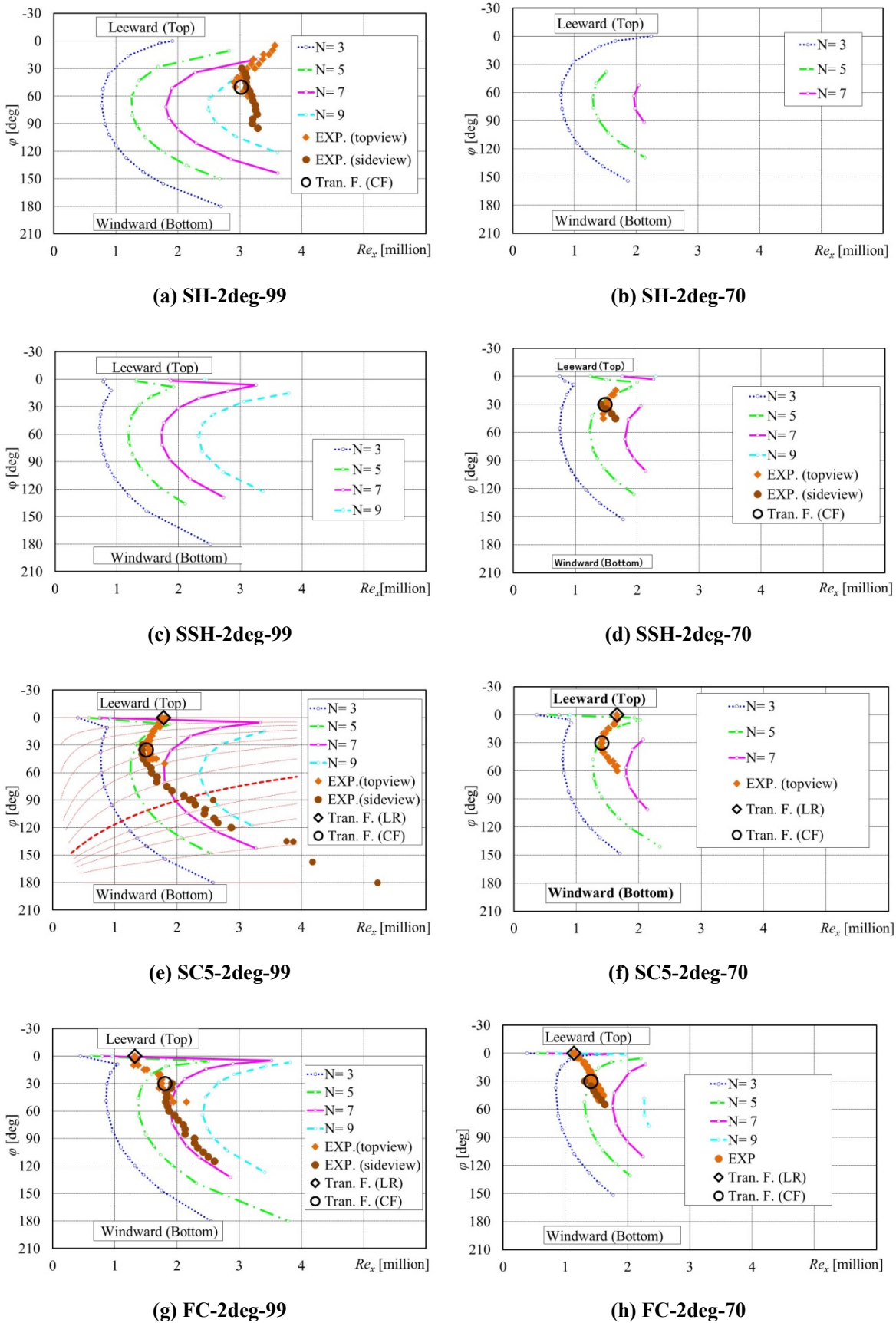
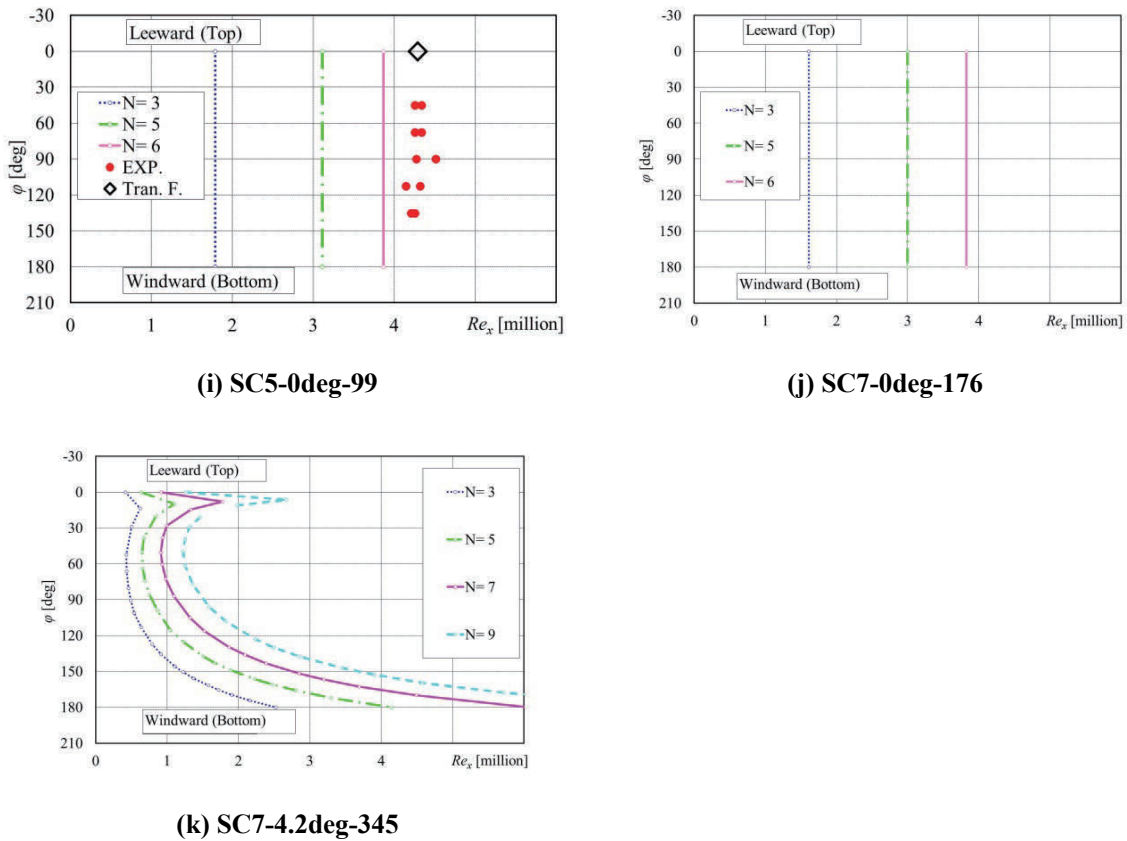


Figure 6.  $N$ -factor contours based on maximum growth envelope method with experimental results.



**Figure 6.  $N$ -factor contours based on maximum growth envelope method with experimental results (completed).**

As shown in Fig. 6(e), the earliest transition in the SC5-2deg-99 case is predicted to occur along the leeward ray ( $\varphi = 0$  degrees) rather than along the adjoining side surface. The integration trajectories used for  $N$ -factor calculations in this case are also shown in the same figure. The apex (i.e., most upstream location) of the crossflow dominated transition lobes on the side of the cone was found to be located at approximately  $\varphi = 60$  degrees, in agreement with a previous prediction for the same cone at the same Mach number [54, 55]. The farthest downstream onset of transition is predicted to occur along the windward ray, i.e., at  $\varphi = 180$  degrees and this location is farther downstream than the predicted transition for a zero angle of incidence case (Fig. 6(i)).

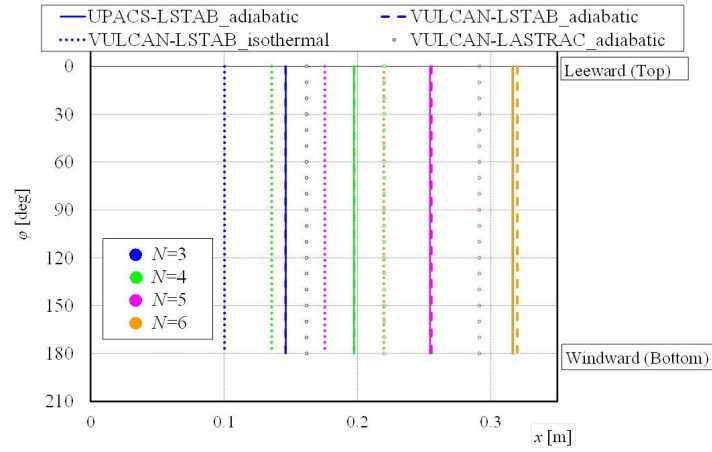
The upstream movement of transition location along the leeward ray and the side area were observed for the SC7-4.2deg-345 (Fig. 6(k)) case, compared with the SC5-2deg-99 case (Fig. 6(e)). On the other hand, the transition location along the windward ray moved to the downstream. Those differences are clearly due to differences of the boundary layer profile depending on the Reynolds number, the cone half angle and the angle of incidence.

On the contrary,  $N$ -factor contours for the straight cone at zero degrees angle of incidence were almost the same regardless of the cone half-angle (Fig. 6(i) and 6(j)) and of the stagnation pressure. This agreement is natural because the boundary layer profiles are very similar as shown in Figs. 3(a) and 3(b). Moreover, the unit Reynolds numbers for both cases are similar (Table 1).

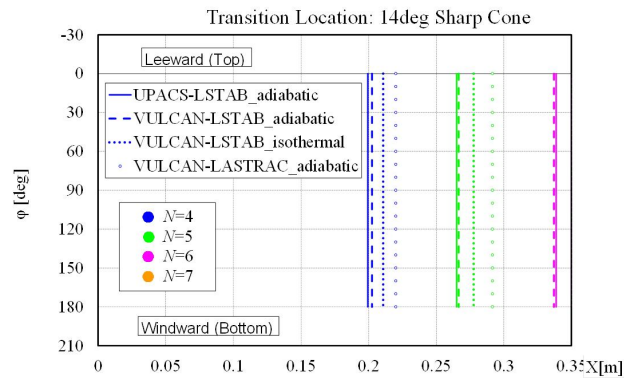
#### 4.4 Comparison of Stability Analysis

An illustrative comparison of  $N$ -factor contours based on the mode tracking method with those obtained with the maximum growth envelope method is shown in Figs. 7. This comparison is made for the SC5-0deg-99, SC7-0deg-176 and SC5-2deg-99 configurations using basic states obtained for an isothermal ( $T_w/T_{ad} \approx 1.08$ ) model surface; however, to illustrate the effect of the thermal boundary conditions, the results of the maximum growth envelope method for the adiabatic mean flow are also included. For the adiabatic case, results obtained using two different mean flow solvers (VULCAN and UPACS, respectively) but the same stability code (LSTAB) are shown. Because the adiabatic mean flow profiles predicted by VULCAN and UPACS are in close agreement with each other, the resulting stability predictions are also very close to each other.

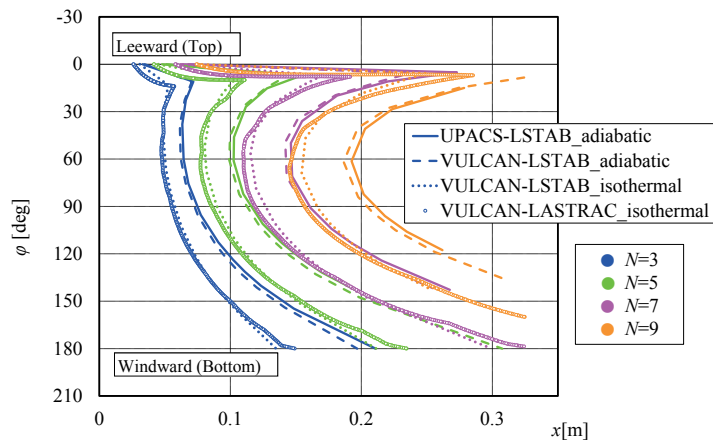
Figure 7 also shows that, for the SC5-2deg-99 configuration at least, the  $N$ -factor contours predicted by the maximum growth envelope method are similar to those predicted by the mode tracking method, but there are some small differences between the two sets of predictions because of the different assumptions in computing the  $N$ -factor curves. On the other hand, the thermal boundary condition has a larger impact on the  $N$ -factor contours, especially away from the leeward plane of symmetry. The upstream shift in  $N$ -factor contours for the isothermal case reflects the destabilizing effect of increased wall temperature on both first mode and crossflow instabilities. The isothermal condition effectively leads to an increase in  $N$ -factor of between 1 and 2 in this case. These results may be concluded as follows: the most important point to predict transition location by use of  $e^N$  methodology is the use of the same thermal condition for the mean flow computation. The capability to predict transition location is confirmed, when the same thermal condition and the  $N$ -factor value is used.



(a) SC5-0deg-99



(b) SC7-0deg-176



(c) SC5-2deg-99

Figure 7. Comparison of  $N$ -factor contours.

## 5 Method and Results of Experiments

### 5.1 Wind Tunnel Facilities

The wind tunnel experiments were conducted by JAXA in two different facilities, with the lead author of this paper as the principal investigator. The measurements in each facility provided information about the transition front over the model as well as the static pressure fluctuations in the free stream.

The first facility was the 0.2m×0.2m supersonic wind tunnel (SWT2) at JAXA. [64]. The SWT2 tunnel nozzle has been designed using the method of characteristics and the contraction ratio to the cross-sectional area of the test section is 28.3. A boundary layer suction device is mounted at the contraction in order to provide a low disturbance flow. However, it was not used because the device is not effective in stabilizing the wall boundary layer. A total of 4 screens were employed to avoid flow separation and to establish better flow uniformity. The SWT2 is a continuous flow facility that allows independent and continuous variations in both Mach number ( $1.5 < M_\infty < 2.5$ ) and total pressure ( $55 \text{ kPa} < P_0 < 100 \text{ kPa}$ ). The nominally controlled total flow temperature  $T_0$  equals 335 K, but can be increased if necessary by terminating the supply of the cooling water. For the work described in this paper, the flow conditions for all tests in SWT2 were fixed at  $M_\infty = 2$ ,  $P_0 = 70 \text{ kPa}$ , and  $T_0 = 335 \text{ K}$ . In other words, the test condition of  $P_0 = 99 \text{ kPa}$  for the FWT measurements could not be repeated during the measurements in SWT2 because the capacity of the SWT2 cooling system is rather low to allow continuous operation at the fixed nominal temperature of  $T_0 = 335 \text{ K}$  at the flow condition of interest.

The second facility used in the present work was the 0.6m×0.6m High Speed Wind Tunnel at Fuji Heavy Industries in Japan, which is an in-draft type facility. It will be denoted as FWT in this paper. This wind tunnel nozzle has been also designed using the method of characteristics in conjunction with a correction for boundary layer displacement. A total of 3 screens were employed. The freestream Mach number in FWT can be varied in steps, and was maintained at  $M_\infty = 2$  for the experiments reported herein. The total pressure  $P_0$  and total temperature  $T_0$  are almost atmospheric but cannot be prescribed. Therefore, the  $P_0$  and  $T_0$  values vary from run to run; however, the magnitudes of these variations are small, with the resulting variation in the unit Reynolds number being less than 5% and a dew point temperature of less than 258 K.

For transition measurements, the original schlieren window in both wind tunnels was replaced by a sapphire-glass window to enable the measurement of model surface temperature using an infrared (IR) camera at both facilities.

Neither SWT2 nor FWT incorporate any form of boundary layer control to delay transition in the nozzle wall boundary layer. Hence, as in other conventional supersonic facilities, the tunnel disturbance environment is expected to include a substantial component due to the acoustic radiation from the turbulent boundary layers along the tunnel walls. Somewhat surprisingly, however, the free-stream static pressure fluctuations in both facilities have been found to be rather low at the test Mach number of  $M_\infty = 2$  ( $p'_{\text{RMS}} < 0.1\%$  in SWT2 and  $p'_{\text{RMS}} = 0.04\%$  for FWT). Here,  $p'_{\text{RMS}}$

denotes the root-mean-square value of the surface pressure fluctuation scaled by the dynamic pressure of the free-stream and was measured using a Kulite pressure transducer mounted on a straight cone model at zero degrees angle of incidence.

The measured static pressure fluctuations were lower than those quoted in Refs. 49 and 64 in spite of the wider frequency bandwidth of the present measurement. The Kulite XCS-062 pressure transducer with a diameter of 1.6 mm has a resonance frequency of 150 kHz and a nominal bandwidth of 0 kHz to 50 kHz. However, because of an uncalibrated amplifier, the net estimated bandwidth of the unsteady pressure measurements is limited to the frequency range of 0 kHz to 30 kHz. The cause for this discrepancy from the earlier measurements has not been determined. The static pressure fluctuations in the FWT are comparable to those measured in flight at similar Mach numbers; however, the level of vortical fluctuations and their impact on transition in these facilities remains unknown.

Given the low amplitudes of free-stream acoustic disturbances, both facilities were deemed acceptable, at least for studying the mechanisms for transition within the boundary layer flow along the leeward symmetry plane. As an additional *a posteriori* assessment of the tunnel disturbance environment, the transition Reynolds numbers for axisymmetric flow past a straight cone in SWT2 and FWT were compared with those in other conventional and low disturbance (i.e., quiet) wind tunnel facilities as well as those measured in a flight experiment. This comparison indicated that the transition behavior in SWT2 and FWT is effectively similar to that in other conventional wind tunnels in spite of the lower levels of free-stream pressure fluctuations in these two facilities. This finding also suggests that the nonacoustic disturbance environment in these facilities (which has not been measured) is likely to have a significant influence on the transition process, but also that the overall flow quality is comparable to that in other conventional tunnels.

## 5.2 Test Models

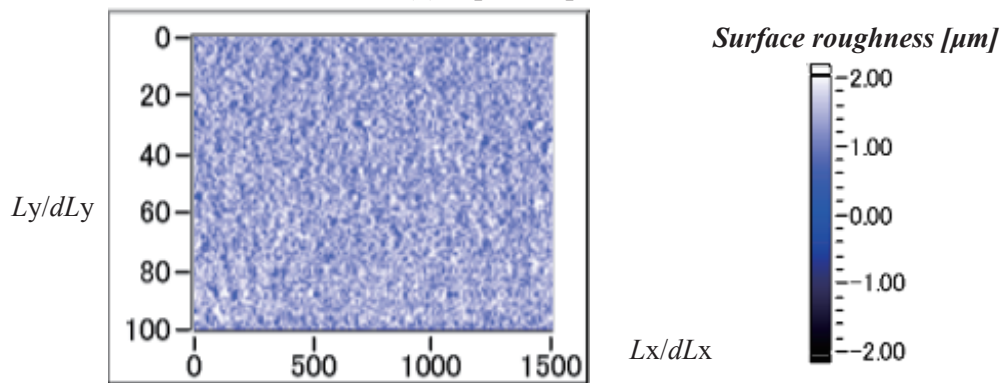
The geometric specifications of the four test models used for transition measurements were summarized in Table 1. Each model was made of polysulfone (PSU) with a stainless steel core. Since the polysulfone resin was not suitable to process the sharp apex, the latter was made of stainless steel. The aft end of the cone that connects with the model sting was also made of stainless steel. All models incorporate a yawing mechanism in order to vary the yaw angle in wind tunnels that do not have a  $\beta$ -sting. Since the yawing mechanism is very small, it does not affect the flow quality. A longer straight cone model with a total axial length of  $L = 0.7$  m was used at FWT. On the other hand, the shorter straight cone model with a total axial length of  $L = 0.3$  m was used at SWT2 (Fig. 8(a)). The length of all of the other models was 0.33 m. All models had a  $\beta$ -sting function in the form of a hinge that enabled the cone to be set at a nonzero yaw angle if necessary. The  $\beta$ -sting function permitted the observation of leeward and windward views from the side.



(a) Appearance of model.



(b) Apex shape.



(c) Reproduced surface roughness

Figure 8. Experimental model of SC5 ( $L = 0.3$  m).

To measure the surface pressure fluctuation  $p'_{\text{RMS}}$ , a Kulite sensor was flush-mounted. The axial locations of the transducers are different for each model. A total of 4 sensors are mounted on the straight cone model of  $L = 0.7$  m, all of which are located downstream of  $x = 450$  mm. On the straight cone model of  $L = 0.3$  m, however, two sensors are mounted on opposite sides of the model at  $x = 150$  mm ( $\varphi = 90$  deg) and  $x = 250$  mm ( $\varphi = -90$  deg), respectively. A single sensor was mounted at  $x = 170$  mm and  $\varphi = 180$  deg. on each of the FC, SH, and SSH models. Since the azimuthal locations are different for each test, those are described for each result.

The apex shape was examined through micrographs and was found to have significant azimuthal variations. The apex diameter is defined as the diameter of a circular fit to the apex shape, averaged over photographs taken from four different directions. The apex diameter determined in this manner was found to be different for each model, with the overall range being  $41 \mu\text{m}$  to  $260 \mu\text{m}$  (Fig. 8 (b)). The nonzero apex diameter is likely to influence the stability and transition processes, especially on models with a larger nose diameter. However, it was not possible to model these effects during the computations performed in this study.

Due care was taken to minimize any surface height discontinuities at the juncture between the nose and the main part of cone. The juncture was finished following the assembly of the two parts. Therefore, resulting discontinuities over the actual test article are sufficiently small, such that there is no difference between the tactile impressions on either side. Hence, the magnitude of juncture discontinuities is estimated to be nearly the same as that of the surface roughness, which was estimated by reproducing the roughness pattern on small samples of dental resin (Pattern Resin 1-1PKG). The resin was hardened together with a paper backing that could be easily peeled off with the help of a hole at the center of the paper. The reproduced roughness on the resin sample was measured with a laser displacement sensor (LT-8010; Keyence). The roughness amplitudes (measured as arithmetic mean of roughness heights) for all four models were nearly the same, approximately in the range of  $0.6 \mu\text{m} \sim 0.7 \mu\text{m}$  (Fig. 8 (c)).

The effects of azimuthal variations near the cone apex and the surface roughness on either the mean flow or the disturbance evolution within the downstream region are not addressed in this paper.

### 5.3 Instrumentation and Measurement Methodologies

Since the rate of heat transfer reflects the transport properties of the boundary layer flow, the transition front can be inferred as the locus of points associated with a rapid axial gradient in surface heat transfer. The surface temperature distribution was measured using an infrared camera (TVS-8502, Nippon Avionics Co. Ltd.). This camera provided  $256 \times 236$  pixel images with less than 0.025 K resolution at the rate of 30 Hz. The corresponding spatial resolution depends on the test case, and is from about 0.16 mm to about 1 mm. This data was subsequently converted to a surface heat flux distribution under the assumption of semi-infinite, one-dimensional thermal conduction through a uniform medium with temperature invariant thermal properties. The heat transfer rate  $q_w$  as a function of time  $t$  has been estimated via the following equation: [65]

$$q_w = \sqrt{\frac{\rho C k}{\pi}} \left\{ \frac{T(t)}{\sqrt{t}} + \int_0^t \frac{T(t) - T(\tau)}{(t - \tau)^{3/2}} d\tau \right\} \quad (5)$$

where  $T(t)$  denotes the surface temperature at time  $t$ , and  $\rho$ ,  $C$  and  $k$  denote the density, the specific heat and the thermal conductivity of the material, respectively. To reduce high frequency noise compared with the period of flow change (typically 60 seconds for SWT2 tests and 10 seconds for FWT tests),  $T(t)$  was approximated by a moving average over a time interval of 5 seconds for SWT2 tests and 1 second for FWT tests, where the averaging intervals are approximately one order of magnitude smaller than the corresponding period of interest. Because of the relatively low thermal diffusivity of the insulative material of the model, the Fourier number ( $F = \kappa t / (\rho C R^2)$ ) based on the thickness of the model (i.e., the local model radius  $R$ ) remained less than 0.04 over the duration of the IR measurement. It suggests the length scale of the lateral thermal diffusion corresponds to a Fourier number of 1. The low Fourier number implies not only that the penetration depth through the IR measurement is sufficiently shallow to support the assumption of semi-infinite model thickness during the reduction of the measured temperature data, but also that the length scale of lateral

thermal diffusion is small compared with the radius of the model. For the tests conducted in FWT, the initial surface temperature distribution can be reasonably assumed to be uniform. However, because of the long duration of the tests conducted in the closed circuit wind tunnel SWT2, the temperature distribution at the model surface had nearly reached an equilibrium at the start of the IR measurement and, therefore, the surface heat flux was very small. To obtain a measurable heat flux, a small but sudden, i.e., step-like change, was applied to the SWT2 stagnation temperature ( $\Delta T_0 \approx 5$  K) after reaching the equilibrium temperature distribution for  $T_0 \approx 335$  K. This change in stagnation temperature occurred during a time interval of less than 100 seconds. The 5-degree variation in stagnation temperature is negligible from the standpoint of comparison with the numerical prediction, since it corresponds to a unit Reynolds number variation of just 2%. The measured changes in surface temperature in response to the change in  $T_0$  were used in conjunction with Eq. 5 to estimate the heat transfer rates during the SWT2 tests. The initial temperature in this case was obtained from the measured distribution of equilibrium temperature before the step-like change in stagnation temperature was applied. An analogous technique for IR-based transition measurements was used during a recent flight experiment involving crossflow transition at a low subsonic Mach number. The heat transfer distributions inferred via the procedure outlined above are shown in Fig. 9, where the transition front is clearly marked by a sharp, negative axial gradient in the images corresponding to the measurements in FWT and by a sharp positive gradient for the images acquired in the SWT2. The reason behind the opposite gradients in heat transfer distributions in the two facilities is clarified in subsection 5.4 below. Such opposite gradients can be reconciled using a comparison based on the Stanton number distribution, which yields similar trends in both facilities as expected. However, deducing the Stanton number from the heat flux requires the knowledge of stagnation temperature corresponding to each IR image and, unfortunately, the stagnation temperature measurement was not synchronized with the IR measurement. The resulting uncertainty in the stagnation temperature prevents a comparison between the measured heat flux and the CFD results.

Phosphor thermography and temperature-sensitive-paint (TSP) techniques are commonly utilized for transition detection in high-speed boundary layers. However, compared to these techniques, measurements using an IR camera have the advantage that it does not affect the smoothness of the measurement surface. Maintaining the surface finish is particularly important for the present study because of the potential significance of stationary crossflow instability for transition over the side region of the cone models (i.e., away from the symmetry planes). The stationary crossflow modes can be easily excited by surface roughness, such as that introduced by the application of the phosphor coating or the TSP. Hence, the latter two measurement techniques can artificially influence the natural transition process over the body surface and thus, were not used during the current study.

Surface pressure fluctuations on the SC5 model of  $L = 0.3$  m at  $x = 150$  mm were measured by flush-mounted Kulite sensors (XCS-062) at  $\varphi = 0$  deg and  $\varphi = 180$  deg. The sensor has a diameter

of 1.6 mm. The acquired signal was analyzed using a 16-bit multi-functional digital FFT analyzer (CF-5210; ONO-SOKKI).

#### 5.4 Pattern of Heat Transfer Distribution

Heat transfer maps for the test conditions of interest are shown in Figs. 9(a) through 9(h). All figures were observation from a top view perspective. However, the centerline of the images is not along the leeward ray of the model due to the physical limitations of the camera installation in order to avoid the reflection of the cooling system of the IR-camera itself. The Kulite sensor on the shorter SC is located downstream of the  $x = 450$  mm location, i.e., beyond the axial region included in the IR image from Fig. 9(e). On the SC5 model, the upstream sensor was located at  $\varphi = 90$  deg. and the downstream sensor was at  $\varphi = -90$  deg. in Fig. 9(f) for the SC5-2deg-70 configuration and located at  $\varphi = 180$  deg. on each of the FC, SH, and SSH models. The presence of these sensors did not have any influence on the temperature distributions in Figs. 9. Even though the edge of the model is less clear against the background of the surrounding tunnel wall, the latter was retained in order to avoid any artificial manipulations of the acquired image. The yellow arrows in each of these figures indicate the location of an aluminum tape that was used as a fiduciary mark along the rear section of the model. The tape thickness was of the order of tens of micrometers. It was placed significantly farther downstream of the transition location and the edges of the tape were pressed down carefully in order to minimize any upstream influence. Therefore, virtually no influence was observed on the transition location. For example, an asymmetric transition pattern was not observed even when the tape was mounted asymmetrically. To allow an estimation of the cone length captured within each image, a pair of thin black horizontal arrows is used in each figure (with the exception of Fig. 9(c)) to indicate a reference length along the model axis. The absence of this pair of arrows in Fig. 9(c) is due to the low accuracy of the reference aluminum tape in the SSH-2deg-99 case. In this case, the aluminum tape (which was prepared before the experiment) was too far downstream of the transition location and, hence, was not included within the IR image. As a temporary fix, therefore, another tape was used to help determine an approximate location of transition.

It may be noted that the distributions of heat transfer at  $P_0 = 70$  kPa and  $P_0 = 99$  kPa have opposite signs. The data at  $P_0 = 70$  kPa was acquired in SWT2 by terminating the cooling water to apply a step-like change in the stagnation temperature of the flow as mentioned above. As a result, the direction of heat transfer is from the flow to the model surface (i.e.,  $q_w > 0$ ). On the other hand, the model temperature for the  $P_0 = 99$  kPa runs in the short duration facility, FWT, is higher than the adiabatic surface temperature and, therefore, the flow cools the model, i.e.,  $q_w < 0$ . Nevertheless, in both cases, the transition location corresponds to a rapid rise in the magnitude of the surface heat flux from an upstream region of lower and slowly varying heat transfer to a downstream region of higher (and, again, slowly varying) heat transfer. In this manner, the heat transfer maps in Fig. 9 may be used to make some qualitative estimates concerning the expected shape of the transition front. Quantitatively inferred transition fronts using a combination of the top view images in Fig. 9 and

side view images obtained by rotating the cone (which are not shown in this paper) are described in subsection 5.5 below.

For the SH body, transition at  $P_0 = 99$  kPa is first seen to occur over the side of the cone, i.e., away from the leeward plane of symmetry (Fig. 9(a)). There is actually a local maximum in the transition location along the leeward ray, so that the overall shape of the transition front on the unrolled surface of the SH body (such that the leeward ray is located along the center) resembles a “W” shape that has been rotated counterclockwise by 90 degrees. Henceforth, this shape will be referred to as the “sideways W” pattern. The upstream transition over the side region is believed to have been caused by crossflow instabilities in that region. The shape of this crossflow transition lobe is analogous to that seen previously during quiet tunnel measurements of a Mach 3.5 delta-wing configuration [43] as well as in the course of conventional facility measurements for a yawed circular cone at Mach 6 [59, 65]. The cause of transition along the leeward ray (where the crossflow velocity is identically zero because of symmetry) is not immediately obvious. It could have been initiated by the amplification of linear instabilities of the laminar flow in its vicinity or induced by turbulent contamination from the adjacent region. Figure 9(b) shows that in the lower Reynolds number case SH-2deg-70, the boundary layer flow remained laminar over the entire body surface. Figures 9(c) and 9(d) reveal that, similar to the SH configuration, the SSH body shape also exhibits the “sideways W” shaped transition pattern, with an earlier transition location away from the leeward ray. The main difference between the transition patterns over the two bodies is that for SSH, transition was observed to occur even in the lower Reynolds number case (Fig. 9(d)).

The higher Reynolds number case SC5-2deg-99 (Fig. 9(e)) for the straight cone configuration indicates a qualitative change from the transition pattern observed for the SH and SSH body shapes. The transition front in this case appears to include an additional, narrow lobe centered on the leeward ray. Since there is no crossflow along the leeward ray, the center lobe (which is still small for the SC5-2deg-99 case, but becomes more prominent for the FC configurations in Figs. 9(g) and 9(h)) is attributed to a different transition mechanism than the crossflow effects underlying the outer two lobes within the transition front. Because the earliest transition location within the center lobe occurs along the leeward ray, one may reasonably assume that the underlying cause of transition is the amplification of instabilities along the leeward ray. It is seen, however, that the transition location along the leeward ray is still significantly farther downstream from the earliest onset of transition within the side region. This may be due to the fact that for  $\alpha = 2$  degrees, the secondary flow leading to the thickening of the leeward symmetry plane boundary layer is still relatively weak at the unit Reynolds number corresponding to this case (SC5-2deg-99).

The three lobed transition front observed in the higher Reynolds number straight cone case (SC5-2deg-99) is also observed in both high and low Reynolds number cases involving the flared cone (Figs. 9(g)-(h)). Furthermore, the transition front for both FC cases indicates a marked reversal in the relative axial positions of the center lobe and the outer lobes respectively, in comparison with the high Reynolds number straight cone case discussed earlier (Fig. 9(e)). In particular, the initial

onset of transition along the center lobe is now significantly upstream in comparison to the transition location anywhere along the outer lobes. Overall, the transition front images from Fig. 9 indicate a progressively stronger transition mechanism along the leeward ray as the axial pressure gradient becomes increasingly less favorable in going from the SH body (modestly favorable) to FC (modestly adverse).

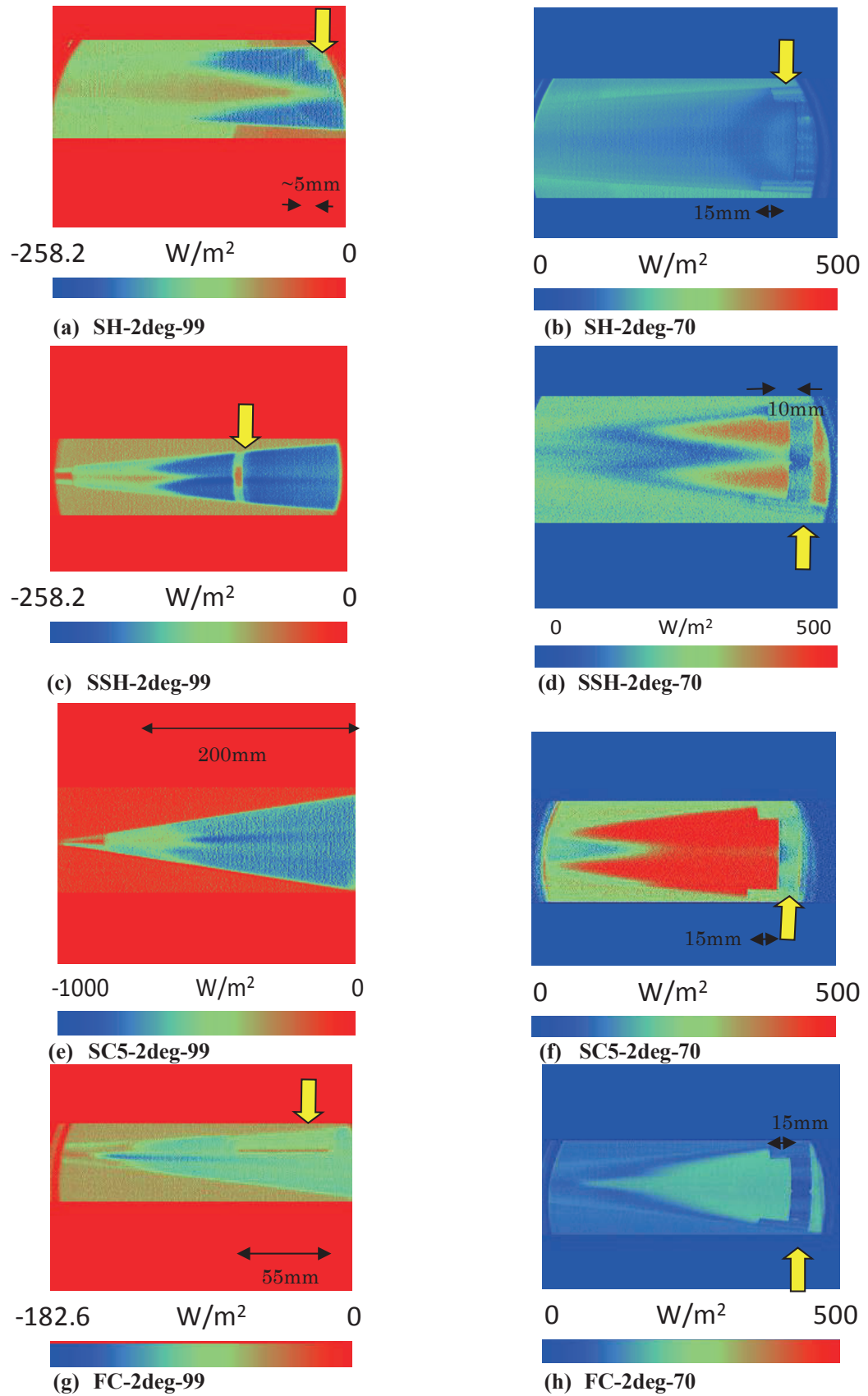


Figure 9. Heat transfer distributions for test conditions of interest (top view, approximately centered on the leeward symmetry plane). Figures in the left-hand-side were obtained in FWT, and those in the right-hand-side were obtained in SWT2.

### 5.5 Extraction of Transition Location

The maps of heat transfer from the previous subsection outlined the qualitative nature of transition patterns over the canonical nose configurations of interest. The present subsection describes quantitative estimates of the transition front in the relevant cases. The transition location was extracted from the maps of “temperature difference ( $\Delta T$ )” between two selected instants of time for a given run. For the short duration tests carried out in FWT, the two selected times correspond, respectively, to the time  $t = t_1$  when the flow condition was stabilized in FWT and some later instant  $t = t_2$  ( $t_2 > t_1$ ) when a measurable temperature difference had been established with respect to  $t = t_1$ . The corresponding times for the tests in SWT2 are based on the beginning and the end of the surface temperature response to the step-like change in stagnation temperature.

Axial variations in  $\Delta T$  along selected cone generators (corresponding to lines of constant azimuthal angle along the cone surface) are extracted from the surface maps of  $\Delta T$  using the location of an aluminum tape as a reference as mentioned previously. The extraction of a selected cone generators is explained in detail in Appendix A.

For each curve of this type, the transition region and the laminar and turbulent flow regions immediately upstream and downstream of the transition region are each approximated by a linear segment (Fig. 10). The point of intersection between the laminar and transitional segments corresponds to the onset of transition, whereas the point of intersection between the transitional and turbulent segments defines the end of transition. The midpoint of the straight line segment connecting the onset- and end-of-transition locations defines the midpoint of the transition zone. The midpoint locus is used as the measured transition location in the remainder of this paper. The extracted transition location is shown in Figure 11.

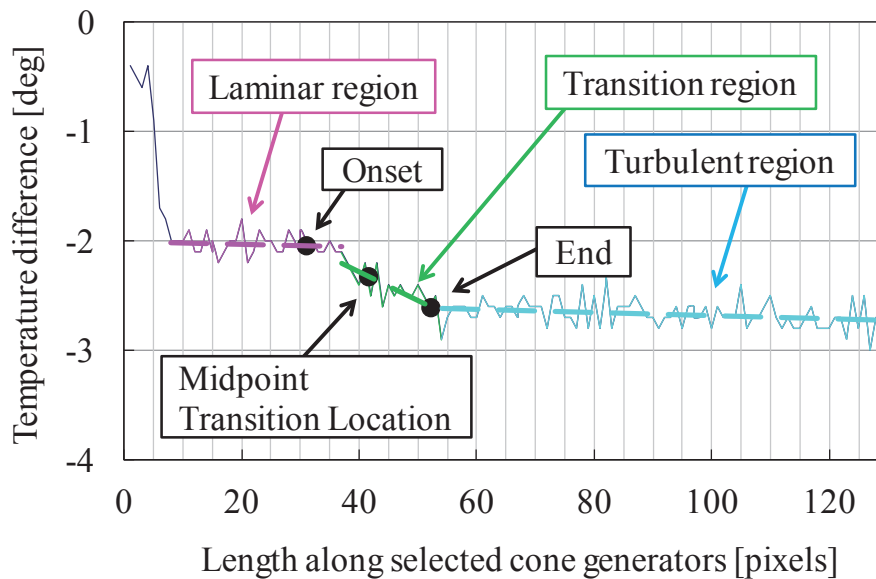


**Figure 10. Sample variation of temperature difference along a line of constant azimuthal angle ( $\phi = 30$  deg of FC-2deg-99).**

The extracted transition for the 7 cases from Table 1 are shown in Figs. 6(a) and (d)-(i).

The uncertainty in experimentally inferred transition locations was estimated to be less than approximately  $\pm 5$  mm. This estimate includes the combined effect of the finite resolution of the IR image, the uncertainty in the identification of transition location from the IR image, and the uncertainty in the correspondence between the IR-image and the physical location on the model. The light brown circles in Fig. 6 indicate the transition front based on the top view of the model, whereas the dark brown circles in Fig. 6 indicate the transition front inferred from the side view of the model, though the side-view results are not shown in this paper. The opposite side transition location obtained from the top view is superimposed at the corresponding azimuthal location in the figure. Since the superimposed data at  $\varphi < 0$  deg overlap the data at  $\varphi > 0$  deg, no significant asymmetry was observed. The transition locations in the side view images (not shown) was acquired independently, but under the same flow conditions. In order to obtain the side view data, the model was rotated by 90 degrees. There are clear but modest differences between the transition fronts inferred from the two views of each model. These differences reflect the uncertainty in mapping the IR image to surface coordinates. The factors contributing to this uncertainty include: curvature of the model surface, possible inaccuracy in the location(s) of the aluminum tape used as a fiducial mark, and inadequate resolution of the IR images. It may be noted that transition fronts for the SH-2deg-70 and the SSH-2deg-99 cases were not extracted, since transition did not occur for the SH-2deg-70 case. For the SSH-2deg-99 case, the accuracy of the reference aluminum tape was also rather low as mentioned above. On the other hand, the transition location is not extracted in the leeward ray region for the SSH-2deg-70 case, since it occurs very far downstream and cannot be extracted from the IR measurement. The open diamond and circle in Figs. 6(a) and (d)-(h) correspond, respectively, to transition locations along the leeward ray and the minimum of the crossflow transition lobe on the side, as described below.

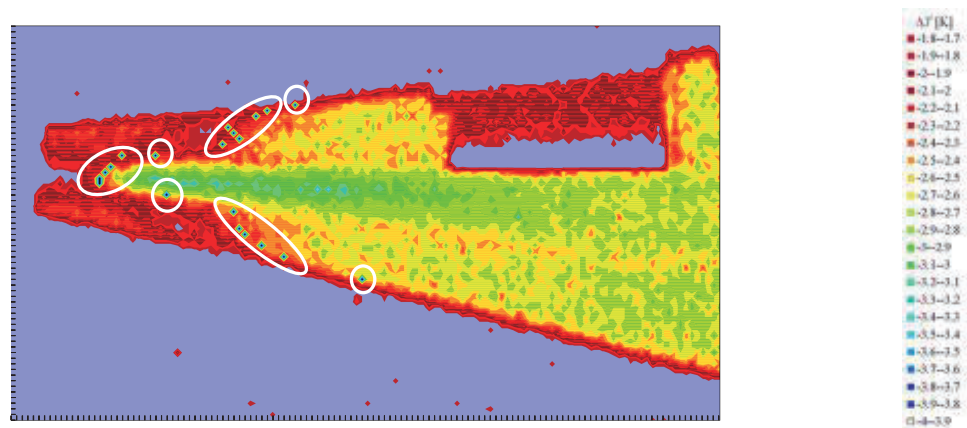


Figure 11. Extracted transition locations (FC-2deg-99).

## 5.6 Comparison with numerical prediction

Next, two separate scalar measures of the overall transition front are extracted from the results shown in Figs. 6. These two measures correspond, respectively, to the transition location on the leeward ray and the earliest location of the side lobe associated with crossflow transition. The values

of both measures for each of the relevant cases are summarized in Table 2, wherein  $Re_x$  denotes the local Reynolds number based on free-stream velocity and kinematic viscosity at the inferred transition location. Because of the previously mentioned discrepancies between transition fronts based on the side and top views, the values of the scalar measures are averaged over the two views as necessary. The transition locations for the FC-2deg-99 and the FC-2deg-70 configurations are monotonically increasing functions of the azimuthal angle  $\varphi$  from the leeward ray and, hence, the minimum of the side lobe could not be identified. Therefore, the location at  $\varphi = 30$  degrees is listed in the Table. The transition front measures extracted in this manner are shown in Figs. 6(a)-(i) by a large black open diamond and circle, respectively.

The transition Reynolds number of 4.29 million for the straight cone at zero angle of incidence falls between the range of transition Reynolds numbers observed in previous flight experiments at Mach 2 and conventional wind tunnel measurements for slightly higher Mach numbers ( $M_\infty = 2.5$  to 4.0) but similar values of unit Reynolds number [53, 54]. The fact that the measured transition Reynolds numbers are considerably lower than those in flight [62] cannot be easily reconciled with the low values of measured free-stream pressure fluctuations in the SWT2 and the FWT facilities. A more detailed study of the free-stream disturbance environment may help explain this finding.

The experimentally observed transition front with occurrence of a center lobe in the transition front over the SC and FC bodies and its absence over the SSH body at  $P_0 = 99$  kPa is in agreement with the predicted transition fronts. The absence of early transition along the leeward ray is an open question. However, while the measured transition front for the SSH body showed later transition along the leeward ray, the corresponding  $N$ -factor contours do predict a local minimum in the transition location along the leeward ray. This discrepancy suggests that the simplistic approach of correlating multiple transition mechanisms using a single  $N$ -factor value is not realistic for this flow and that the  $N$ -factor value correlating with crossflow induced transition over the side region is sufficiently smaller than the  $N$ -factor value correlating with transition due to first mode instability along the leeward ray. Such differences in  $N$ -factor correlations are easily possible due to differences in receptivity characteristics as well as nonlinear mechanisms related to the respective underlying instability mechanisms. An alternate hypothesis, which is explored in Ref. 58, is that the classical stability theory cannot capture the entire physics of instability evolution along the leeward ray and a more advanced prediction approach based on a partial-differential-equation-based planar (i.e., two-dimensional) eigenvalue analysis may be necessary in this case. An additional difference between the predicted  $N$ -factor contours and the measured transition fronts corresponds to the weaker signature of the outer (crossflow) lobe in the measured transition front over the FC (Figs. 9(g) and 9(h)), such that there is a nearly monotonic downstream shift in the measured transition location at increasing azimuthal angles from the leeward ray. This might have happened because the boundary layer flow along the azimuthal orientations corresponding to the inner portions of the crossflow transition lobes transitioned further upstream due to turbulent contamination from the earlier transition location along the leeward ray.

The numerically predicted  $N$ -factor values at the measured transition locations along the leeward ray and the farthest upstream location of the crossflow transition lobe (see Figs. 6) for the various flow configurations are summarized in Table 2. It may be observed that the  $N$ -factors at the transition location along the leeward ray are always greater than 13.5 and, hence, are much higher than the  $N$ -factor value of 6.2 correlating with measured transition under axisymmetric conditions. Quiet tunnel measurements [51] for axisymmetric flow over a cone indicate  $N$ -factor values of 9 to 10. The finding that  $N = 6.2$  under zero angle-of-incidence conditions can be explained by the fact that conventional tunnels yield lower correlating  $N$ -factors than quiet tunnels. On the other hand, the increase in  $N$ -factor for transition along the leeward ray is much too large to be explained by the fact that the measured transition location is based on the middle of the transition zone rather than with the transition onset location (which is only about 10 percent upstream compared to the midpoint of the transition zone).

One possible reason for the extraordinarily high  $N$ -factors for leeward plane transition could be related to potential differences between the computed and actual boundary layer profiles due to a lack of sufficient information concerning the imperfections of the model tip and/or flow quality effects such as flow angularity, etc. However, the high  $N$ -factor values are observed for more than one body shape, i.e., two different models with separate nose tips. Furthermore, it is shown in Ref. 2 that analogously high  $N$ -factors are also found for a completely different 5-degree cone model that was used by King [53] during his quiet-tunnel experiments at Mach 3.5. Thus, the effect of nose tip imperfections or flow angularity would appear to be an unlikely explanation for the high  $N$ -factors along the leeward plane. An entirely different explanation involves possible shortcomings of the classical stability theory underlying the  $N$ -factor correlations from Table 2. Specifically, it is possible that the azimuthal gradients of the basic state, although zero along the leeward ray, become large enough in the immediate vicinity of the leeward symmetry plane to influence the disturbance evolution within the leeward plane. These azimuthal gradients are not accounted for in the classical stability theory. An additional contributing factor could be related to potentially weaker receptivity mechanisms for the leeward flow in comparison with those of the axisymmetric boundary layer, perhaps because of the somewhat higher frequencies of the relevant instability modes and the associated decay in the amplitudes of the free-stream disturbances, which could cause a delay in transition and lead to the higher  $N$  factors.

In comparison with the  $N$ -factor values along the leeward symmetry plane, the corresponding  $N$ -factors at the apex of the experimentally inferred transition lobe on the side of the cone models are much lower but comparable to the  $N$ -factor at the measured transition location for first mode transition in the axisymmetric case SC5-0deg-99 (Table 2). The low  $N$ -factor values in the axisymmetric case as well as for the side lobe at the nonzero angle of incidence are comparable to the  $N$ -factor values correlating with previous transition measurements in conventional facilities, in spite of the fact that the measured levels of free-stream acoustic fluctuations in the FWT and SWT2 facilities appear to be much lower than other conventional facilities. The reasons behind the low  $N$ -factors may be related to inaccuracies in determining transition locations from the IR measurement, imperfections in model geometry (anisotropy

of nose tip, curvature discontinuity, and small scale perturbations in surface geometry) and the potential presence of nonacoustic free-stream disturbances.

While the presence of crossflow plays an important role in influencing the amplification of instability modes in the side region, the role of first mode waves and stationary and traveling modes of crossflow instability cannot be established on the basis of available measurements. Indeed, in spite of decades of research involving transition in 3D, high-speed boundary layer flows, this fundamental difficulty is yet to be overcome. The linear stability results plotted in Figs. 6 show that the  $N$ -factor contours in the side region (which are dominated by traveling crossflow instability) indicate rather small variations from one body shape to another. Indeed, for example, the apex of the  $N = 9$  contour within the side region moves by less than 10 percent across the four body shapes considered in this paper. Although not shown, similar insensitivity to axial pressure gradient was also noted in the  $N$ -factor contours for purely stationary crossflow instability. Thus, the most significant effects of axial pressure gradient on boundary layer stability are confined to the vicinity of the leeward plane.

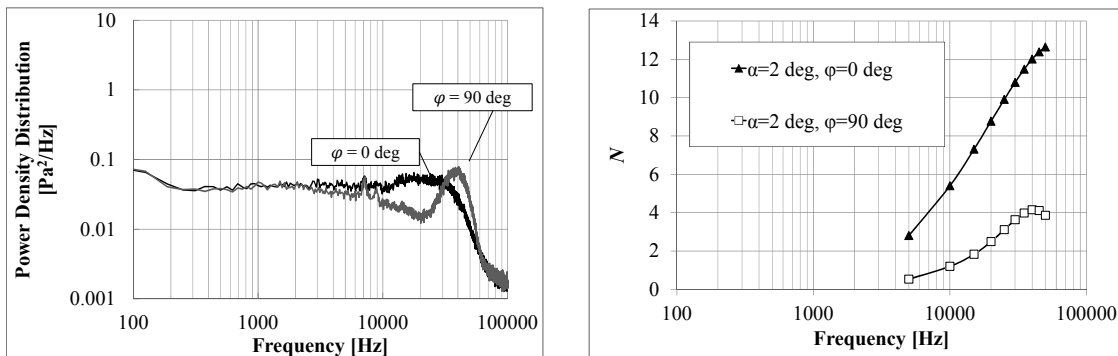
As mentioned above, the precise cause behind transition cannot be established due to the difficulty in making in-depth disturbance measurements. Nonetheless, some limited comparisons could be made between linear stability predictions and the experimental measurements. Surface pressure fluctuations measured using the Kulite sensor can provide potentially useful information concerning boundary layer disturbances at the sensor location [66]. The azimuthal location of the sensor could be varied, allowing one to obtain measurements at multiple values of  $\varphi$ .

**Table 2: Summary of transition locations.**

Shape	$\alpha$ [deg]	$P_0$ [kPa]	Transition front along leeward symmetry plane					Apex of transition front within side region				
			$x$ [m]	$Re_{x,tr}$ [million]	$N$ - LSTAB	$N$ - LASTRAC	comment	$x$ [m]	$Re_{x,tr}$ [million]	$\varphi$ [deg]	$N$ - LSTAB	comment
			SC	0	0.33	4.29	6.2	5.6	extra- polated			
SH	2	99						0.24	3.02	50	9.6	-
SSH												
SC			0.14	1.79	18.4	16.9	-	0.12	1.51	35	5.5	-
FC			0.11	1.32	13.5	10.9	-	0.15	1.80	30	6.2	at 30 deg
SH												
SSH	70							0.21	1.48	30	5.2	-
SC			0.23	1.65	26.4		-	0.19	1.41	30	5.1	-
FC			0.16	1.14	13.6		-	0.19	1.40	30	5.1	at 30 deg

Figure 12(a) shows the frequency spectra of surface pressure fluctuations for three different values of  $\varphi$  in the case of the SC5-2deg-70 configuration. The spectra for  $\varphi = 0$  deg and  $\varphi = 90$  deg reveal high amplitude disturbances within specific frequency bands indicating the presence of potential instability amplification. The frequencies corresponding to the spectral peaks of surface pressure fluctuation at the Kulite location are approximately 20 kHz for  $\varphi = 0$  deg (i.e., the leeward symmetry plane) and 40 kHz when  $\varphi = 90$  deg. Recall that, because of the frequency limitations of the amplifier, the estimated bandwidth of the unsteady pressure measurements is limited to 30 kHz and, therefore, the peak near 40 kHz provides only a qualitative measure of the underlying disturbance amplitudes. At this location, the predicted wave angle is very close to 90 deg with respect to the inviscid flow direction. Therefore, the disturbance is expected to be a traveling crossflow mode. The spectral peak for  $\varphi = 0$  deg is broad, but the increase in amplitude near 20 kHz (relative to the background fluctuations away from the peak) is clearly seen for  $\varphi = 90$  deg. The reason of the broadness for  $\varphi = 0$  deg is an open question.

The frequency of the most amplified disturbances as predicted by the stability analysis was compared with the frequency spectrum of the experimentally observed surface pressure fluctuations. According to the maximum growth envelope method, the most amplified disturbance at the Kulite location had a frequency of more than 50 kHz along the leeward ray and about 40 kHz at  $\varphi = 90$  deg. The predicted frequency agrees reasonably well with the measured spectrum at  $\varphi = 90$  deg, but is larger than the measured peak frequency along the leeward ray.



(a) Frequency spectra of measured surface pressure fluctuations along leeward ray (b) Predicted  $N$ -factors as functions of disturbance frequency

**Figure 12 Comparison between frequency spectra of measured surface pressure fluctuations and the  $N$ -factor predictions as a function of disturbance frequency for the SC5-2deg-70 configuration.**

The precise reason for the discrepancy in disturbance frequencies along the leeward ray could not be determined. However, it might again be related to the various factors that were outlined above in the context of the large  $N$ -factor values along the leeward ray. Kulite measurements were also obtained along the windward ray, but the disturbance amplitudes in the experiment were too small to yield an adequate signal-to-noise ratio; hence, those measurements cannot be compared with the theoretical predictions.

## 6 Summary

Boundary layer transition on axisymmetric bodies at a nonzero angle of incidence in a supersonic freestream was investigated via experiments and numerical computations as part of joint research between the Japan Aerospace Exploration Agency (JAXA) and the National Aeronautics and Space Administration (NASA).

Transition over four axisymmetric bodies (namely, a Sears-Haack body, a semi-Sears-Haack body, two straight cones and a flared cone) with different streamwise pressure gradients was studied. The experimental measurements included visualization of the transition front via heat transfer distributions inferred from the surface temperature measurements using an IR camera, along with limited measurements of surface pressure fluctuations and mean boundary layer profiles along the leeward symmetry plane. The measurements indicate that the boundary layer transition along the leeward symmetry plane may occur earlier than that along the neighboring azimuthal locations, when the streamwise pressure gradient is zero or adverse. The earlier transition along the leeward ray under adverse axial pressure gradients is consistent with the computational predictions, which indicate increasingly thicker and more strongly inflectional (and correspondingly more unstable) boundary layer profiles along the leeward symmetry plane when the streamwise pressure gradient becomes relatively more adverse. The destabilizing effect of pressure gradient on the boundary layer flow within the leeward symmetry plane is analogous to that in purely two-dimensional (or axisymmetric) boundary layer flows at both subsonic and supersonic Mach numbers [67-72]. However, in the present context, the cause behind this destabilizing effect is entirely different, being related to the three-dimensional dynamics involving an increasing build-up of secondary flow along the leeward symmetry plane under an adverse axial pressure gradient. This secondary flow is also shown to induce a strongly dissimilar behavior of boundary layer profiles along the leeward ray even though the boundary layer development over the rest of the cone is nearly self-similar and the instability amplification characteristics in that region are relatively insensitive to the axial pressure gradient. Under zero-angle-of-incidence conditions, the same conical configurations do not display a similarly dramatic effect of body shape on boundary layer stability as observed along the leeward plane under a nonzero angle of incidence. Computations also confirm the weakened instability of the boundary layer flow along the leeward symmetry plane when the axial pressure gradient is sufficiently favorable. However, additional analysis is necessary to establish whether turbulent contamination from the adjacent region of crossflow dominated transition might play a role during transition along the leeward plane under the favorable pressure gradient.

This paper provides the IR-based global measurements of boundary layer transition over a yawed circular cone in the supersonic regime, albeit with a significant uncertainty in the quantitative data pertaining to transition locations. More important, the profound effect of axial pressure gradient on the transition behavior along the leeward symmetry plane of slender axisymmetric bodies at a nonzero angle of incidence has been demonstrated.

The present work has also identified certain discrepancies between the predicted  $N$ -factor contours

and the experimentally observed transition fronts for certain cases, as well as indicating rather high  $N$ -factor values for leeward transition even in a conventional facility. These discrepancies indicate the potential sensitivity of boundary layer transition along the leeward symmetry plane to external disturbances and/or to turbulent contamination, and hence underscore the limitations of  $N$ -factor correlations for boundary layer flow involving multiple instability mechanisms. The need to perform more detailed measurements of leeward line transition, both in terms of basic state profiles and the boundary layer perturbations, especially in a low disturbance environment, is also highlighted by the present findings. Resolving these discrepancies and addressing the need for more definitive measurements are important topics for follow-on work.

### **Acknowledgments**

The JAXA authors would like to express thank for the advice from Dr. K. Yoshida, Dr. T. Atobe, along with the graduate technical trainees, Mr. A. Nose, Mr. T. Murayama, Mr. K. Fujisaki, Ms. T. Osada from Gakushuin University and Mr. T. Kawai, Ms. A. Tozuka from Aoyama-Gakuin University.

Majority of the work at NASA was performed as part of the Supersonic Cruise Efficiency -- Airframe discipline of the Supersonics Project of the NASA's Fundamental Aeronautics Program (FAP); however, the documentation of results was completed under support from Revolutionary Computational AeroSciences element of the Transformational Tools and Technologies Project. Technical discussions with Ms. K. Berger, Mr. S. A. Berry, Dr. M. Malik, Dr. R. Rubinstein, Ms. E. Lee-Rausch, Mr. S. Wilkinson, Mr. L. Owens, and Dr. P. Balakumar at NASA Langley Research Center are also acknowledged.

## References

- [1] N. Tokugawa, M. Choudhari, H. Ishikawa, Y. Ueda, T. Atobe, K. Fujii, F. Li, C.-L. Chang and J. A. White, "Transition Along Leeward Ray of Axisymmetric Bodies at Incidence In Supersonic Flow," AIAA Paper 2012-3259 (2012).
- [2] M. Choudhari, N. Tokugawa, F. Li, C.-L. Chang, J. A. White, H. Ishikawa, Y. Ueda, T. Atobe and K. Fujii, "Computational Investigation of Supersonic Boundary Layer Transition over Canonical Fuselage Nose Configurations," *Proceedings of 7th International Conference on Computational Fluid Dynamics*, ICCFD7-2306 (2012).
- [3] N. Tokugawa, M. Choudhari, H. Ishikawa, Y. Ueda, T. Atobe, K. Fujii, F. Li, C.-L. Chang and J. A. White, "Pressure Gradient Effects on Supersonic Transition over Axisymmetric Bodies at Incidence", *AIAA Journal*, **53** (2015), pp. 3737-3751.
- [4] H. Ishikawa, N. Tokugawa, M. Choudhari, F. Li, C.-L. Chang and J. White, "Mean-Flow Computation for Axisymmetric Bodies at Incidence in Supersonic Flow - Progress Report of JAXA-NASA Joint Research Project on Supersonic Boundary Layer Transition (Part 1)," *JAXA-RR-17-002E*, 2017.
- [5] K. F. Stetson, E. R. Thompson, J. C. Donaldson and L. G. Siler, "Laminar Boundary Layer Stability Experiments on a Cone at Mach 8, Part 5: Tests with Cooled Model," AIAA Paper 89-1895 (1989).
- [6] D. W. Bechert, M. Bruse, W. Hage, J. G. T. Van-Der-Hoeven and G. Hoppe, "Experiments on Drag-Reducing Surfaces and Their Optimization with an Adjustable Geometry," *Journal of Fluid Mech.*, **338** (1997), PP.59-87.
- [7] S. G. Anders and M. C. Fischer, "F-16XL-2 Supersonic Laminar Flow Control Flight Test Experiment," NASA TP-1999-209683 (1999).
- [8] L. A. Marshall, "Boundary -Layer Transition Results from the F-16XL-2 Supersonic Laminar Flow Control Experiment," NASA TM-1999-209013 (1999).
- [9] B. R. Kramer, B. C. Smith, J. P. Heid, G. K. Noffz, D. M. Richwine, and T. Ng, "Drag Reduction Experiments Using Boundary Layer Heating," AIAA Paper 1999-0134 (1999).
- [10] A. Wortman, "Reduction of Fuselage Form Drag by Vortex Flows," *Journal. of Aircraft*, **36** (1999), pp. 501-506.
- [11] W. S. Saric, and H., L. Reed, "Supersonic Laminar Flow Control on Swept Wings Using Distributed Roughness," AIAA Paper 2002-0147 (2002).
- [12] P. R. Viswanath, "Aircraft Viscous Drag Reduction Using Riblets," *Prog. In Aero. Sci.*, **38** (2002), pp. 571-600.
- [13] D. Arnal, C. G. Unckel, J. Krier, J. M. Sousa, and S. Hein, "Supersonic Laminar Flow Control Studies in The SUPERTRAC Project," *Proceedings of 25th Congress of International Council of the Aeronautical Science*, 2006-2.9.1 (2006).
- [14] J. Peltzer, J. Suttan, and W. Nitsche, "Applications of Different Measuring Techniques for Transition Detection in Low and High Speed Flight Experiments," *Proceedings of 25th*

- Congress of International Council of the Aeronautical Science*, 2006-3.3.1 (2006).
- [15] S. Sinha and S. V. Ravande, "Drag Reduction of Natural Laminar Flow Airfoils with a Flexible Surface Deturbulator", AIAA Paper 2006-3030 (2006).
- [16] P. Sturdza, "Extensive Supersonic Natural Laminar Flow on The Aerion Business Jet", AIAA Paper 2007-0685 (2007).
- [17] F. Collier, R. Thomas, C. Burley, C. Nickol, C.-M. Lee, and M. Tong, "Environmentally Responsible Aviation - Real Solutions for Environmental Challenges Facing Aviation," *Proceedings of 27th Congress of International Council of the Aeronautical Science*, 2010-1.6.1 (2010).
- [18] H. Hansen, "Laminar Flow Technology - The Airbus View," *Proceedings of 27th Congress of International Council of the Aeronautical Science*, 2010-1.9.4 (2010).
- [19] J. König and T. Hellstrom, "The Clean Sky Smart Fixed Wing Aircraft Integrated Technology Demonstrator: Technology Targets and Project Status," *Proceedings of 27th Congress of International Council of the Aeronautical Science*, 2010-5.9.3 (2010).
- [20] E. Iuliano, R. Donelli, D. Qualiarella, I Salah El Din and D. Arnal, "Natural Laminar Flow Design of a Supersonic Transport Jet Wing-Body," AIAA Paper 2009-1279 (2009).
- [21] J. K. Viken, W. Pfenninger and R. J. Mcghee, "Advanced Natural Laminar Flow Airfoil with High Lift to Drag Ratio," *Langley Symposium on Aerodynamics*, (1986), pp. 401-414.
- [22] A.G. Powell, S. Agrawal, and T. R. Lacey, "Feasibility and Benefits of Laminar Flow Control on Supersonic Cruise Airplanes," *NASA CR-181817* (1989).
- [23] H. D. Fuhrmann, "Applications of Natural Laminar Flow to Supersonic Transport Concept," AIAA Paper 93-3467 (1993)
- [24] R. D. Joslin, "Aircraft Laminar Flow Control," *Ann. Rev. of Fluid Mech.*, **30** (1998), pp. 1-29.
- [25] U. Cella, D. Quagliarella, R. Donelli, and B. Imperatore, "Design and Test of the UW-5006 Transonic Natural-Laminar-Flow Wing", *Journal. of Aircraft*, **47** (2010), PP. 783-795.
- [26] L. Deng and Z. D. Qiao, "A Multipoint Inverse Design Approach of Natural Laminar Flow Airfoils," *Proceedings of 27th Congress of International Council of the Aeronautical Science*, 2010-2.10.5 (2010).
- [27] K. Matsushima, T. Iwamiya, and H. Ishikawa, "Supersonic Inverse Design of Wings for The Full Configuration of Japanese SST," *Proceedings of 22nd Congress of International Council of the Aeronautical Science*, 2000-2.1.3 (2000)
- [28] K. Matsushima, T. Iwamiya, K. Nakahashi, "Wing Design for Supersonic Transport Using Integral Equation Method," *Engineering Analysis with Boundary Elements*, **28**, (2004), pp. 247-255.
- [29] K. Yoshida, D. Y. Kwak, N. Tokugawa and H. Ishikawa, "Concluding Report of Flight Test Data Analysis on The Supersonic Experimental Airplane of NEXST Program by JAXA", *Proceedings of 27th Congress of International Council of the Aeronautical Science*, 2010-2.8.2 (2010).

- [30] N. Tokugawa, D. Y. Kwak, K. Yoshoda and Y. Ueda, "Transition Measurement of Natural Laminar Flow Wing on Supersonic Experimental Airplane NEXST-1," *Journal of Aircraft*, **45** (2008), pp. 1495-1504.
- [31] M. Fujino, "Development of Hondajet," *Proceedings of 24th Congress of International Council of the Aeronautical Science*, 2004-1.7.2 (2004).
- [32] M. Fujino, "Design and Development of the Honda Jet," *Journal. of Aircraft*, **42** (2005), pp. 755-764.
- [33] M. F. Zedan, A. A. Seif, and S. Al-Moufafi, "Drag Reduction of Airplane Fuselage Through Shaping by The Inverse Method," *Journal of Aircraft*, **31** (1994), pp. 279-287.
- [34] N. W. Schaeffler, B. G. Allan, C. Lienard, and A. L. Pape, "Progress Towards Fuselage Drag Reduction via Active Flow Control: A Combined CFD and Experimental Effort," *Proceedings of 36th European Rotorcraft Forum* (2010).
- [35] S. S. Dodbele, C. P. Van Dam and P. M. H. W. Vijgen, "Design of Fuselage Shapes for Natural Laminar Flow," *NASA CP-3970* (1986).
- [36] S. S. Dodbele, C. P. Van Dam and P. M. H. W. Vijgen, B. J. Holmes, "Shaping of Airplane Fuselages for Minimum Drag," *Journal. of Aircraft*, **24** (1987), pp. 298-304.
- [37] P. M. H. W. Vijgen, and B. J. Holmes, "Experimental and Numerical Analyses of Laminar Boundary-Layer Flow Stability over an Aircraft Fuselage Forebody," *Research in Natural Laminar Flow and Laminar-Flow Control, Part 3, NASA CP-2487* (1987), pp. 861-886.
- [38] P. M. H. W. Vijgen, S. S. Dodbele, B. J. Holmes and C. P. Van Dam, "Effects of Compressibility on Design of Subsonic Fuselages for Natural Laminar Flow," *Journal of Aircraft*, **25** (1988), PP. 776-782.
- [39] S. S. Dodbele, "Effects of Forebody Geometry on Subsonic Boundary-Layer Stability", *NASA CR-4314* (1990).
- [40] S. S. Dodbele, "Design Optimization of Natural Laminar Flow Bodies in Compressible Flow," *Journal of Aircraft*, **29** (1992), pp. 343-347.
- [41] T. Lutz and S. Wagner, "Drag Reduction and Shape Optimization of Airship Bodies," *Journal of Aircraft*, **35** (1998), pp. 345-351.
- [42] W. Garvey, "Aerion Still Seeking Manufacturer for Its Supersonic Bizjet Design," *Aviation Week & Space Technology* (2009), pp. 25-26.
- [43] L. N. Cattafesta, III, J. A. Masad, V. Iyer, R. A. King, and J. R. Dagenhart, "Three-Dimensional Boundary-Layer Transition on a Swept Wing at Mach 3.5," *AIAA Journal*, **33** (1995), pp. 2032-2037.
- [44] P. C. Stainback, "Effect of Unit Reynolds Number, Nose Bluntness, Angle of Attack and Roughness on Transition on a 5deg Half-Angle Cone at Mach 8," *NASA TN-D-4961* (1969).
- [45] W. Ladoon and S. P. Schneider, "Measurements of Controlled Wave Packets at Mach 4 on a Cone at Angle of Attack," *AIAA Paper 98-0436* (1998).
- [46] I. Rosenboom, S. Hein and U. Dallmann, "Influence of Nose Bluntness on Boundary -Layer

- Instabilities in Hypersonic Cone Flows,” AIAA Paper 99-3591 (1999).
- [47] T. J. Horvath, S. A. Berry, B. R. Hollis, C.-L. Chang and B. A. Singer, “Boundary Layer Transition on Slender Cones in Conventional and Low Disturbance Mach 6 Wind Tunnels,” AIAA Paper 2002-2743 (2002).
- [48] P. Balakumar, “Receptivity of Supersonic Boundary Layers Due to Acoustic Disturbances over Blunt Cones,” AIAA Paper 2007-4491 (2007).
- [49] P. Balakumar, “Stability of Supersonic Boundary Layers on a Cone at an Angle of Attack,” AIAA Paper 2009-3555 (2009).
- [50] N. S. Dougherty and D. F. Fisher, “Boundary Layer Transition on a 10-Degree Cone: Wind Tunnel/Flight Data Correlation”, AIAA Paper 80-0154 (1980).
- [51] N. S. Dougherty, Jr., and D. F. Fisher, “Boundary Layer Transition Correlation on a Slender Cone in Wind Tunnels and Flight for Indications of Flow Quality,” AEDC TR-81-26, Feb. (1982).
- [52] F.-J. Chen, M. R. Malik, and I. E. Beckwith, “Boundary-Layer Transition on a Cone and Flat Plate at Mach 3.5,” *AIAA Journal*, **27** (1989), PP. 687-693.
- [53] R. A. King, “Three-Dimensional Boundary-Layer Transition on a Cone at Mach 3.5,” *Experiments in Fluids*, **13** (1992), PP. 305-314.
- [54] M. Malik and P. Balakumar, “Instability and Transition in Three Dimensional Supersonic Boundary Layers,” AIAA Paper 92-5049 (1992).
- [55] Y. Ueda, H. Ishikawa and K. Yoshida, “Three Dimensional Boundary Layer Transition Analysis in Supersonic Flow Using a Navier-Stokes Code,” *Proceedings of 24th Congress of International Council of the Aeronautical Science*, 2004-2.8.2 (2004).
- [56] T. C. Lin and S. G., Rubin, “Viscous Flow over a Cone at Moderate Incidence. Part 2. Supersonic Boundary Layer,” *Journal of Fluid Mechanics*, **59** (1973), pp. 593-620.
- [57] H. Sugiura, N. Tokugawa, A. Nishizawa, Y. Ueda, H. Ishikawa, and K. Yoshida, “Boundary-Layer Transition on Axisymmetric Bodies with Angles of Attack in Supersonic Flow,” *Proceedings of 2003 Annual Meeting, Japan Society of Fluid Mechanics* (2003), pp. 352-353, (In Japanese).
- [58] K. Berger, S. Rufer, R. Kimmel and D. Adamczak, “Aerothermodynamic Characteristics of Boundary Layer Transition and Trip Effectiveness of the Hifire Flight 5 Vehicle,” AIAA Paper 2009-4055, (2009).
- [59] M. Choudhari, C.-L. Chang, T. Jentink, F. Li, K. Berger, G. Candler and R. L Kimmel, “Transition Analysis for The HIFiRE-5 Vehicle,” AIAA Paper 2009-4056, (2009).
- [60] A. Nose, H. Ishikawa, Y. Ueda, T. Murayama, and N. Tokugawa, “Influence of The Pressure Gradient on Compressive Boundary-Layer Transition on an Axisymmetric Body at Incidence,” *Proceedings of 2007 Annual Meeting, Japan Society of Fluid Mechanics*, [CD-Rom], (2007), In Japanese.
- [61] H. Yamazaki, S. Enomoto, and K. Yamamoto, “A Common CFD Platform UPACS,” *High*

- Performance Computing Lecture Notes in Computer Science*, **1940** (2000), pp. 182-190.
- [62] D. K. Litton, J. R. Edwards and J. A. White, "Algorithmic Enhancements to The Vulcan Navier-Stokes Solver," AIAA Paper 2003-3979, (2003).
- [63] C.-L. Chang, "LASTRAC.3d: Transition Prediction in 3D Boundary Layers," AIAA Paper 2004-2542, (2004).
- [64] H. Sawada, T. Kohno, and T. Kunimasu, "Pressure Fluctuation Measurements in the NAL 0.2-m Supersonic Wind Tunnel," AIAA Paper 98-0636, (1998).
- [65] W. J. Cook and E. J. Felderman, "Reduction of Data from Thin-Film Heat-Transfer Gages: A Concise Numerical Technique," *AIAA Journal*, **4** (1966), PP. 561-562.
- [66] N. Tokugawa, "Surface pressure fluctuation on axisymmetric bodies in supersonic flows", JAXA-RM-12-011, (2013), in Japanese.
- [67] A. R. Wazzan, G. Taghavi, and H. Keltner, "Effect of Boundary Layer Growth on Stability of Incompressible Flat Plate Boundary Layer with Pressure Gradient," *Phys. Fluids*, **17** (1974), pp. 1655-1660.
- [68] S. K. Saxena and T. K. Bose, "Numerical Study of Effect of Pressure Gradient on Stability of an Incompressible Boundary Layer," *Phys. Fluids*, **17** (1974), pp. 1910-1912.
- [69] Y. H. Zurigat, A. H. Nayfeh and J. A. Masad, "Effect of Pressure Gradient on the Stability of Compressible Boundary Layers," *AIAA Journal*, **30** (1992), pp. 2204-2211.
- [70] J. A. Masad and Y. H. Zurigat, "Effect of Pressure Gradient on First Mode of Instability in Compressible Boundary Layers," *Phys. Fluids*, **6** (1994), pp. 3945-3953.
- [71] R. Govindarajan and R. Narasimha, "Stability of Spatially Developing Boundary Layers in Pressure Gradients," *Journal of Fluid Mechanics*, **300** (1995), pp. 117-147.
- [72] P. Goulpie, B. G. B. Klingmann and A. Bottaro, "Görtler Vortices in Boundary Layers with Streamwise Pressure Gradient: Linear Theory," *Phys. Fluids*, **8** (1996), pp. 451-459.

**Appendix A: Identification of transition location from surface temperature distribution**

### Identification of transition location from surface temperature distribution - 1

- Since reference aluminum tape is not glued on the model, before the blowing, IR image (Fig. A0d) covered by a paper cone (Fig.A0a) was obtained with the same setup of IR camera. The cover has holes marking typical location in not only x direction but also  $\phi$  direction. The model was pre-heated up by using of hair-dryer to make temperature difference at the mark (Fig. A0d).
- The mark location is copied on the IR images (Fig. A0b), which is obtained during the blowing.
- Transition location is roughly determined at the sharp variation of temperature. In the sample, Fig.A0(c), transition location at  $\phi=90\text{deg}$  (that is on the thick line) is determined about 330mm .



Fig. A0(a)

Instantaneous Surface Temperature only

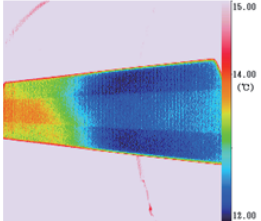
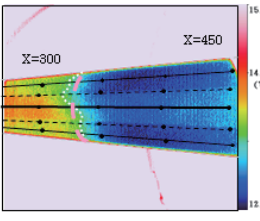
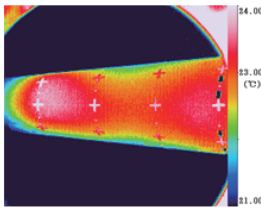




Fig. A0(b)

Fig. A0(c)  
**SC-0deg-99**

Fig. A0(d)

### Identification of transition location from surface temperature distribution - 2

- I. At first, coordinates of 4 points **a, b, c, d**, which is on the generating line from the surface temperature distribution are obtained on the data-processing software as shown in Fig.A1. The generating line is defined at the middle point of rapid the temperature variation along the line which lies at right angles to the generating line and is indicated by red dotted lines in Fig.A1.
- II. Point **e** on the leeward ray is obtained. That is intersection of extrapolated lines a-b and c-d (Fig.A2) . Point **e** would be on the leeward ray. Point **e** is the tip for SC, but not the tip for other bodies, such as SH, SSH and FC.

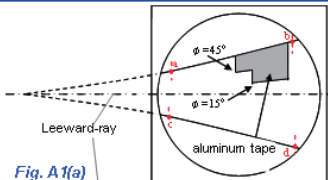


Fig. A1(a)

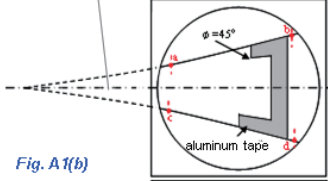


Fig. A1(b)

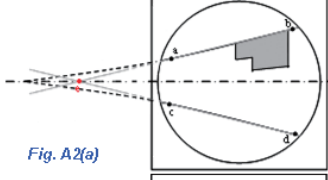


Fig. A2(a)

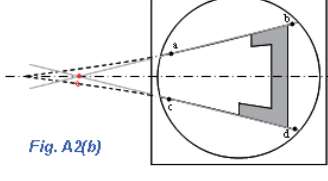


Fig. A2(b)

Leeward-ray

aluminum tape

aluminum tape

### Identification of transition location from surface temperature distribution - 3

- III. Points **f**, **g**, **h**, which are corresponding to the corners of aluminum tape, were obtained as follows (Fig.A3 ). The boundary of aluminum tape was identified at where the sharp variation is observed on temperature along the line across the aluminum tape (red dotted line in Fig.A3 ). Those boundaries are obtained near the corner.
- Then the corner points **f**, **g**, **h** are decided from the locations of boundary in lengthwise and crosswise directions.
- IV. Point **i**, which is on the leeward line, was obtained at the midpoint of **f** and **g** (Fig.A4b). On the other hand, the point **i** was obtained by use of the distance  $\overline{gi}$  from point **g** as follows.

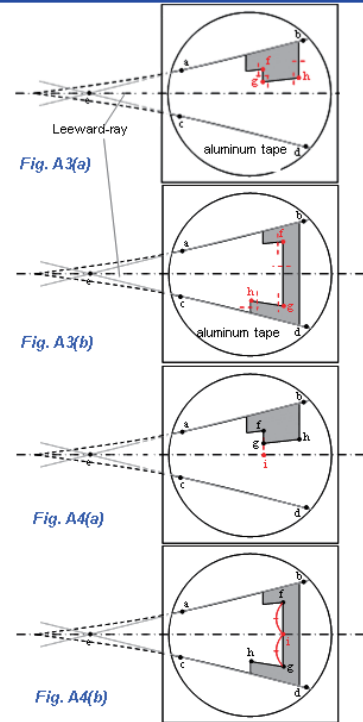
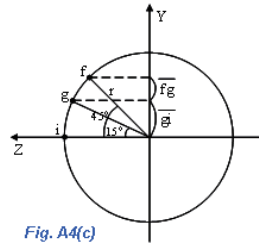
$$\sin 15^\circ = \frac{\overline{gi}}{r}$$

$$\sin 45^\circ = \frac{\overline{fg} + \overline{gi}}{r}$$

$$\overline{fg} = r \sin 45^\circ - r \sin 15^\circ$$

$$r = \frac{\overline{fg}}{\sin 45^\circ - \sin 15^\circ}$$

$$\overline{gi} = \frac{\overline{fg} \sin 15^\circ}{\sin 45^\circ - \sin 15^\circ}$$



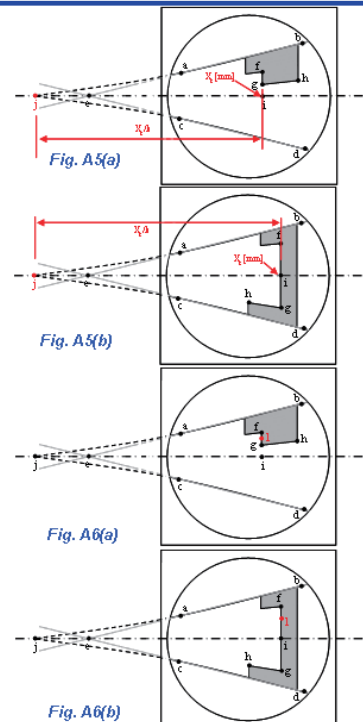
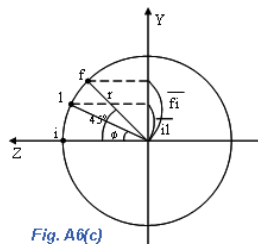
### Identification of transition location from surface temperature distribution - 4

- V. The location of tip **j** is obtained as the ratio of coefficient **k** by axial length of point **i** from the tip **Xg** (Fig.A5 ). Where coefficient **k** is a ratio of actual length to length on data-processing software for infrared images between points **g** and **h**. And axial length of point **i** is same as that of point from **g**. Therefore the length is denoted as **Xg**.
- VI. Point **l**, which locates at arbitrary azimuthal angle  $\phi$  from the leeward-ray and between points **f** and **g** (Fig.A6 ), is decided according to the following equations and Fig.A6(c).

$$r = \frac{\overline{fi}}{\sin 45^\circ}$$

$$\sin \phi = \frac{\overline{il}}{r}$$

$$\overline{il} = r \sin \phi = \frac{\overline{fi} \sin \phi}{\sin 45^\circ}$$



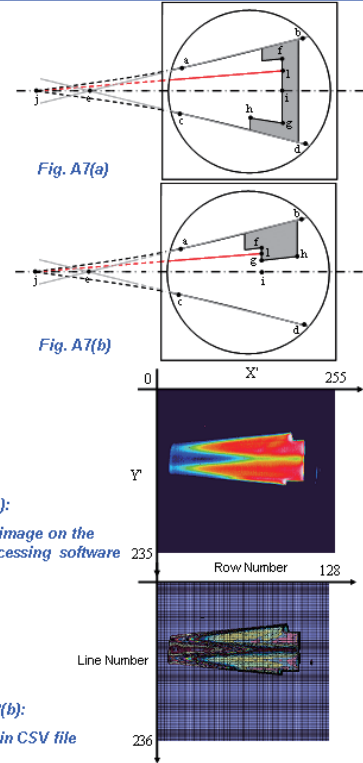
### Identification of transition location from surface temperature distribution - 5

VII. Iso- $\phi$  line was regarded as the straight line between points **g** and **l** (Fig.A5). Iso- $\phi$  line is not straight except straight cone, but the difference is regarded as small and is neglected.

VIII. Infrared image was converted to a CSV file in order to identify transition locations. Since row numbers are absolutely reduced to half through the conversion from infrared image on the data processing software (Fig.A8a) to CSV file (Fig.A8b) unfortunately, the coordinates on the data processing software are exchanged according to the following equation. Since row numbers and line numbers are integer, terms in the right hand side are rounded to the whole number.

$$(RowNumber, LineNumber) = \left( \frac{X'+1}{2}, Y'+1 \right)$$

IX. Points from **a** to **l** and iso- $\phi$  line, obtained until step VII were exchanged corresponding to CSV file on EXCEL.



### Identification of transition location from surface temperature distribution - 6

X. Temperature distribution along the iso- $\phi$  line were drawn (Fig.A9). Temperature variation in laminar, transitional and turbulent regions were approximated as linear. The cross points between laminar-translational regions and translational-turbulent regions were assumed as the onset and end of transition region. And the middle point of onset and end was defined as our transition location.

XI. The transition location on the iso- $\phi$  line was converted as point **m** on the Infrared image as shown in Fig.A10. The transition location is also converted in the actual length ( $X_{TMP}$ [mm],  $Y_{TMP}$ [mm]) as follows (Fig.A11):

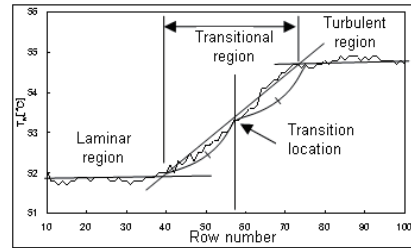


Fig. A9

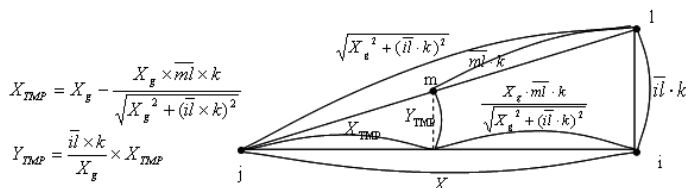
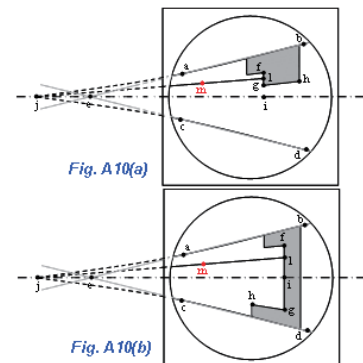
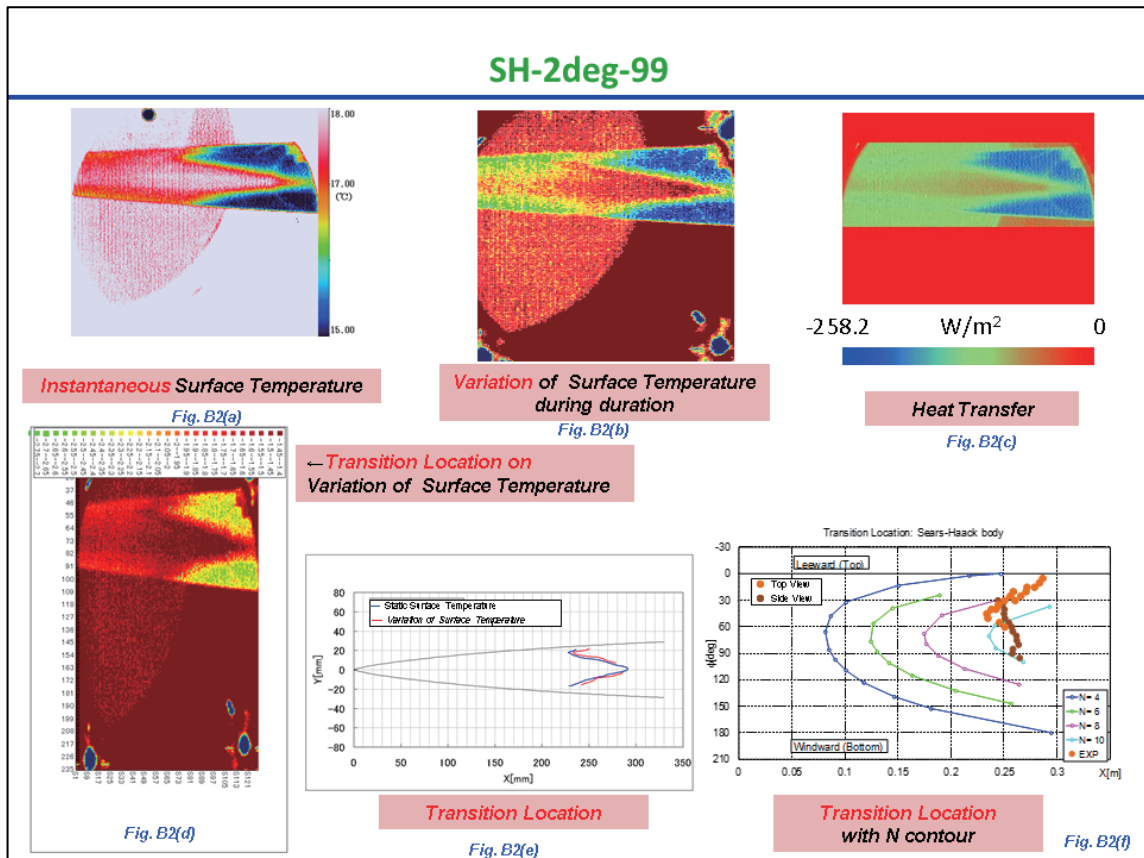
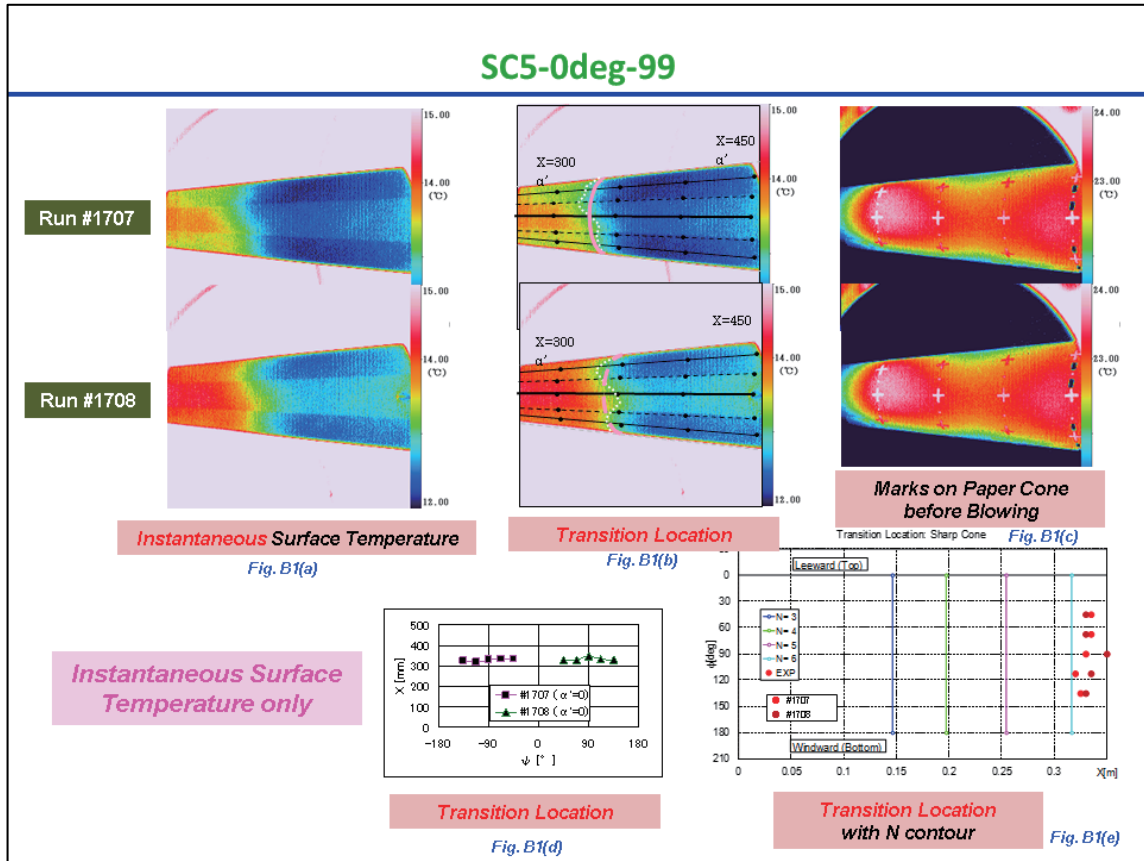
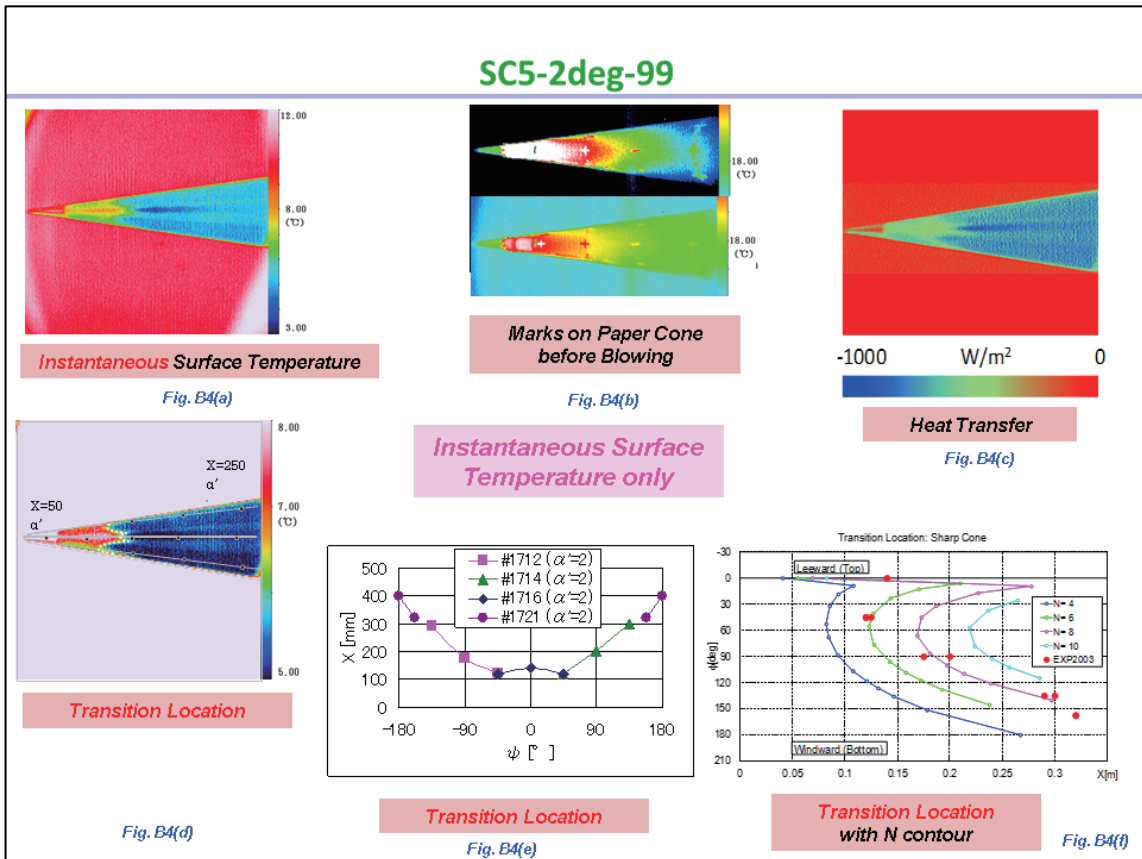
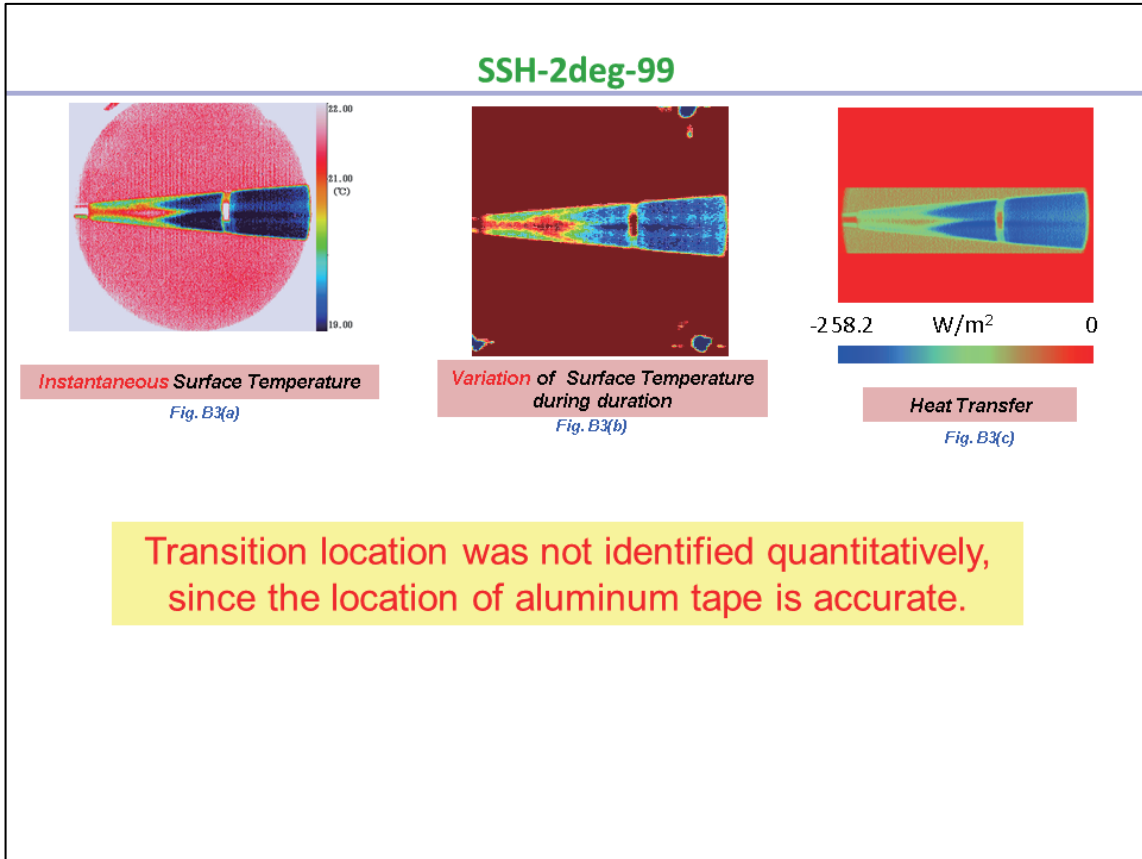
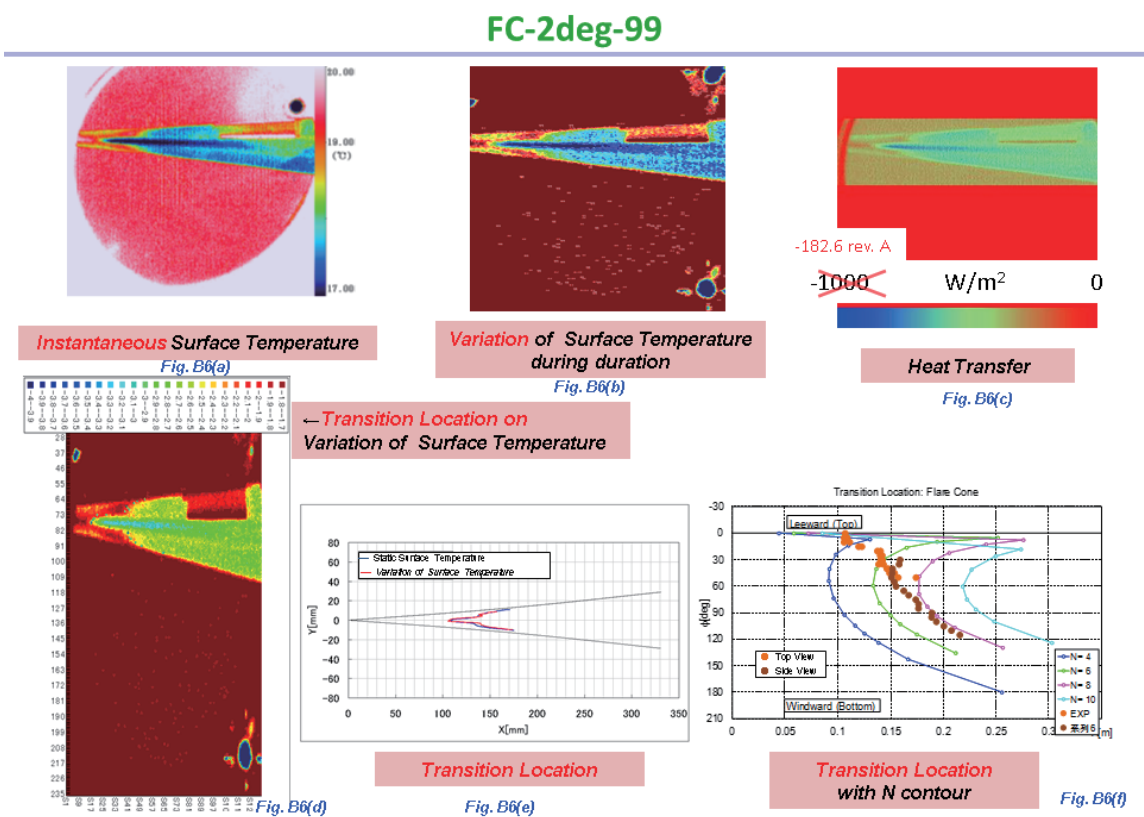
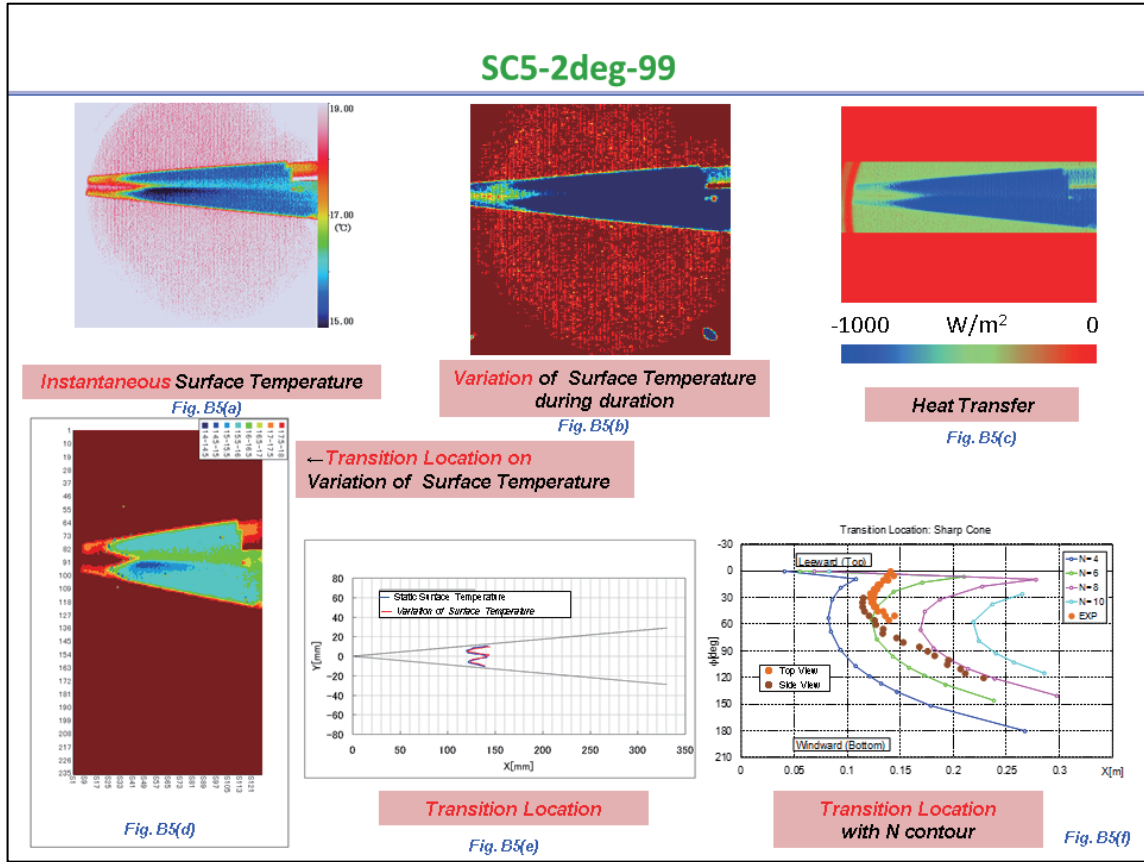


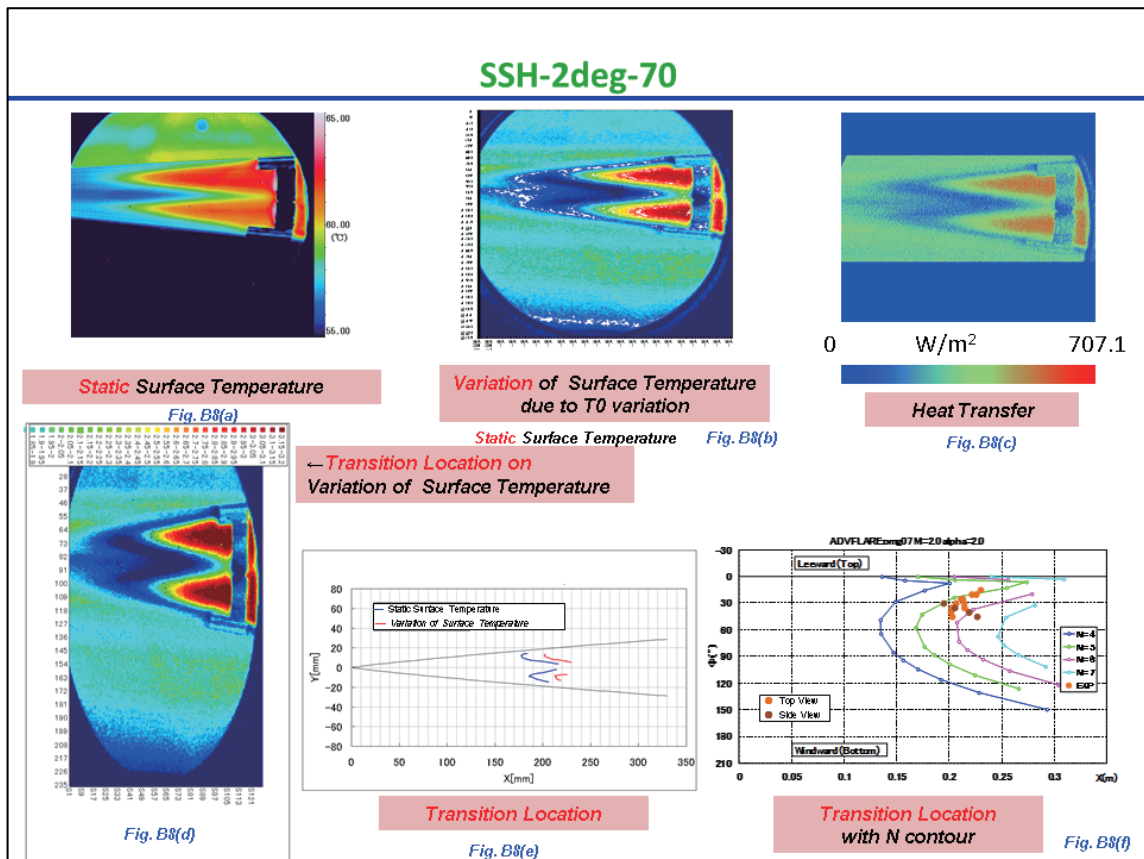
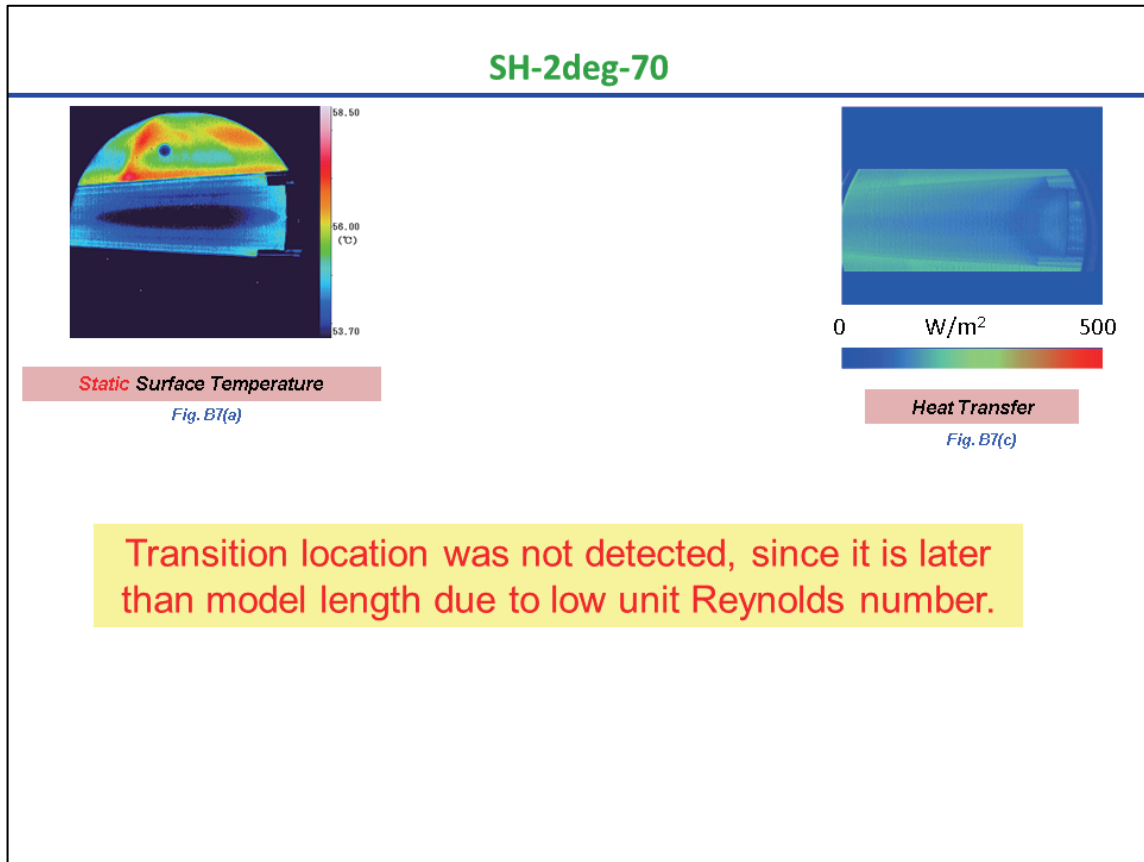
Fig. A11

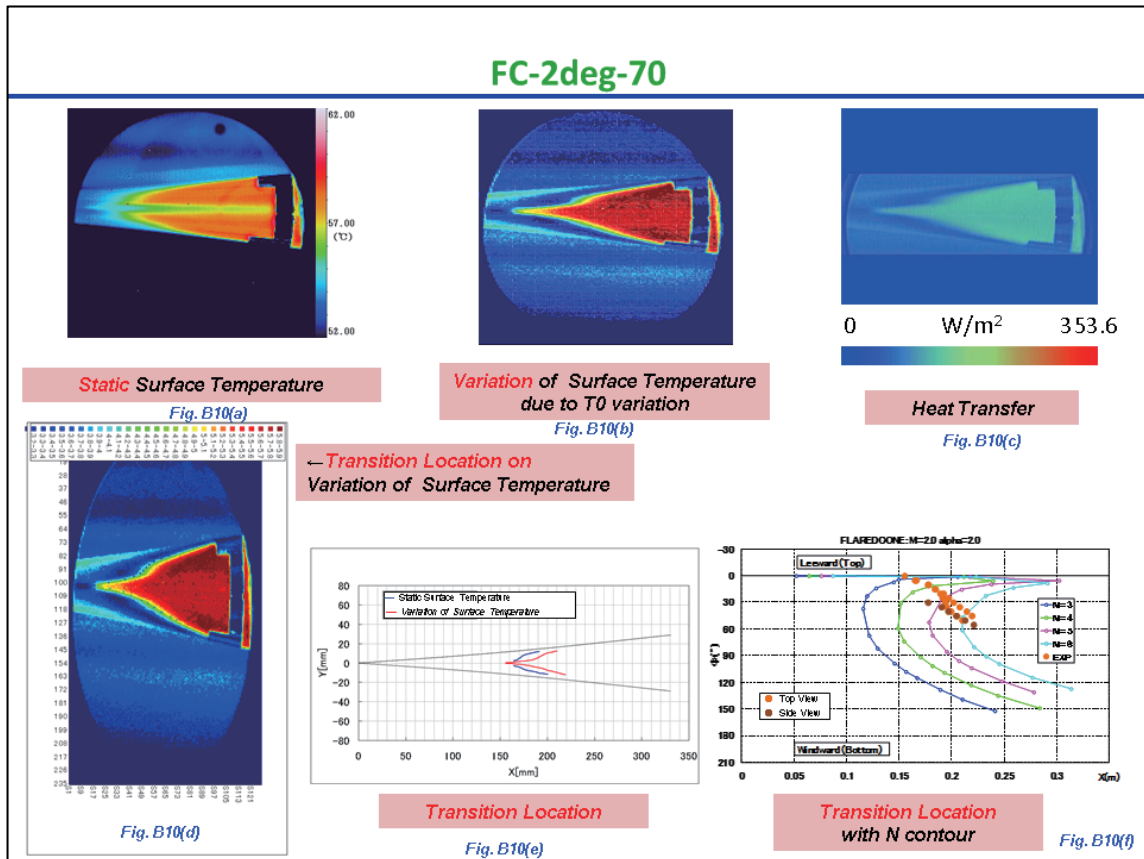
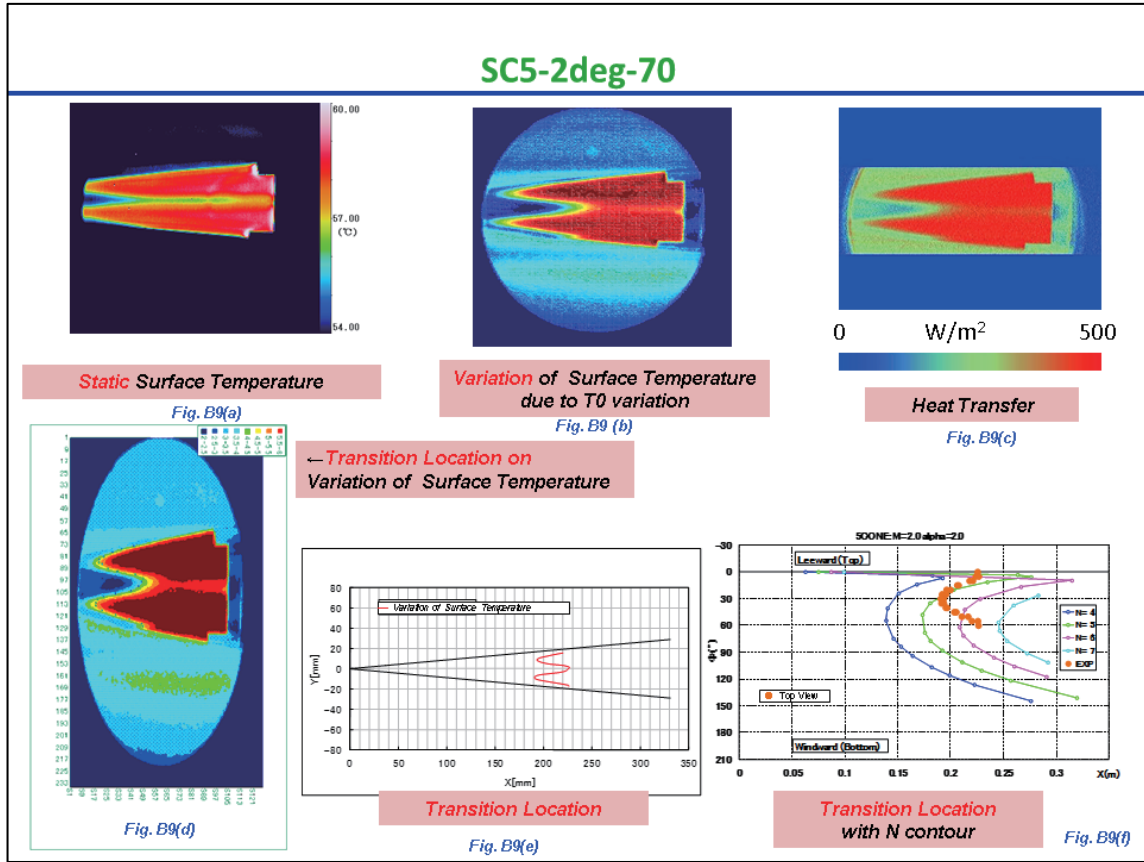
**Appendix B: Identification of transition location from surface temperature distribution**











**JAXA Research and Development Report** JAXA-RR-17-003E

**Pressure Gradient Effects on Transition Location over Axisymmetric Bodies at Incidence in Supersonic Flow**

- Progress Report of JAXA-NASA Joint Research Project on Supersonic Boundary Layer Transition (Part 2) -

---

Edited and Published by: Japan Aerospace Exploration Agency

7-44-1 Jindaiji-higashimachi, Chofu-shi, Tokyo 182-8522 Japan

URL: <http://www.jaxa.jp/>

Date of Issue: September 15, 2017

Produced by: Matsueda Printing Inc.

©2017 JAXA

Unauthorized copying, replication and storage digital media of the contents of this publication, text and images are strictly prohibited. All Rights Reserved.

---

